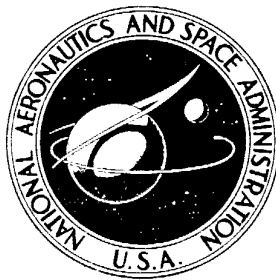


**NASA TECHNICAL  
MEMORANDUM**



**NASA TM X-2419**

**NASA TM X-2419**

**FLIGHT-MEASURED HL-10 LIFTING BODY  
CENTER FIN LOADS AND CONTROL SURFACE  
HINGE MOMENTS AND CORRELATION  
WITH WIND-TUNNEL PREDICTIONS**

*by Ming H. Tang and George P. E. Pearson*

*Flight Research Center*

*Edwards, Calif. 93523*

1. Report No. NASA TM X-2419		2. Government Accession No.		3. Recipient's Catalog No.	
4. Title and Subtitle FLIGHT-MEASURED HL-10 LIFTING BODY CENTER FIN LOADS AND CONTROL SURFACE HINGE MOMENTS AND CORRELATION WITH WIND-TUNNEL PREDICTIONS				5. Report Date October 1971	
				6. Performing Organization Code	
7. Author(s) Ming H. Tang and George P. E. Pearson				8. Performing Organization Report No. H-669	
9. Performing Organization Name and Address NASA Flight Research Center P. O. Box 273 Edwards, California 93523				10. Work Unit No. 126-63-12-00-24	
				11. Contract or Grant No.	
12. Sponsoring Agency Name and Address National Aeronautics and Space Administration Washington, D. C. 20546				13. Type of Report and Period Covered Technical Memorandum	
				14. Sponsoring Agency Code	
15. Supplementary Notes					
16. Abstract  <p style="text-align: center;">Subsonic, transonic, and supersonic aerodynamic loads data are presented for the center fin and the control surfaces of the HL-10 lifting body vehicle. The effects of variations in angle of attack, angle of sideslip, aileron deflection, rudder deflection, and Mach number on the center fin loads are presented in terms of coefficient slopes. The effects of vehicle attitude, control surface deflection, Mach number, and rocket engine operation on the outboard and inboard tip fin flaps, rudder, elevon flap, and elevon hinge-moment coefficients are discussed. The flight test aerodynamic loads are compared with full-scale and small-scale wind-tunnel data.</p>					
17. Key Words (Suggested by Author(s))  Aerodynamic loads  Lifting body vehicle				18. Distribution Statement  Unclassified - Unlimited	
19. Security Classif. (of this report) Unclassified		20. Security Classif. (of this page) Unclassified		21. No. of Pages 38	22. Price* \$3.00

FLIGHT-MEASURED HL-10 LIFTING BODY CENTER FIN LOADS AND CONTROL  
SURFACE HINGE MOMENTS AND CORRELATION WITH WIND-TUNNEL PREDICTIONS

Ming H. Tang and George P. E. Pearson  
Flight Research Center

INTRODUCTION

The concept of maneuverable vehicles capable of controlled reentry from earth orbit to a horizontal landing led to the construction of three manned lifting body configurations to investigate the flight characteristics of these vehicles in the terminal recovery area. As part of the overall lifting body flight test program at the NASA Flight Research Center, detailed aerodynamic load studies (refs. 1 to 3) were made on each of the three configurations: M2-F2, X-24A, and HL-10. A knowledge of the magnitude of the aerodynamic loads and the correlation with wind-tunnel predicted values is important to designers of lifting body vehicles.

This paper presents the center fin loads and control surface hinge moments obtained from the HL-10 flight test program and compares these results with available wind-tunnel predicted loads. The wind-tunnel studies which led to the development of the HL-10 flight vehicle configuration are reported in references 4 to 10.

SYMBOLS

Physical quantities in this report are given in the International System of Units (SI) and parenthetically in U. S. Customary Units. The measurements were taken in U. S. Customary Units. Details concerning the use of SI, together with physical constants and conversion factors, are given in reference 11.

$B$	center fin bending moment, m-N (ft-lb)
$b$	center fin reference span, m (ft)
$C_B$	center fin bending-moment coefficient, $\frac{B}{qS_f b}$
$C_{B_0}$	apparent center fin bending-moment coefficient at $\beta = \delta_a = \delta_r = 0^\circ$
$C_{B_\beta}$	change in center fin bending-moment coefficient with angle of sideslip, $\frac{\partial C_B}{\partial \beta}$ , per deg

$C_{B\delta_a}$	change in center fin bending-moment coefficient with aileron deflection, $\frac{\partial C_B}{\partial \delta_a}$ , per deg
$C_{B\delta_r}$	change in center fin bending-moment coefficient with rudder deflection, $\frac{\partial C_B}{\partial \delta_r}$ , per deg
$C_h$	hinge-moment coefficient, $\frac{HM}{qSc}$
$C_{he_0}$	elevon hinge-moment coefficient at $\alpha = \delta_e = 0^\circ$
$C_{he_\alpha}$	change in elevon hinge-moment coefficient with angle of attack, $\frac{\partial C_{he}}{\partial \alpha}$ , per deg
$C_{he\delta_e}$	change in elevon hinge-moment coefficient with elevon deflection, $\frac{\partial C_{he}}{\partial \delta_e}$ , per deg
$C_{hef_0}$	elevon flap hinge-moment coefficient at $\alpha = \delta_e = 0^\circ$
$C_{hef_\alpha}$	change in elevon flap hinge-moment coefficient with angle of attack, $\frac{\partial C_{hef}}{\partial \alpha}$ , per deg
$C_{hef\delta_e}$	change in elevon flap hinge-moment coefficient with elevon deflection, $\frac{\partial C_{hef}}{\partial \delta_e}$ , per deg
$C_T$	center fin torsion coefficient, $\frac{T}{qS_f \bar{c}}$
$C_{T_0}$	apparent center fin torsion coefficient at $\beta = \delta_a = \delta_r = 0^\circ$
$C_{T\beta}$	change in center fin torsion coefficient with angle of sideslip, $\frac{\partial C_T}{\partial \beta}$ , per deg
$C_{T\delta_a}$	change in center fin torsion coefficient with aileron deflection, $\frac{\partial C_T}{\partial \delta_a}$ , per deg

$C_{T\delta_r}$	change in center fin torsion coefficient with rudder deflection, $\frac{\partial C_T}{\partial \delta_r}$ , per deg
$C_Y$	center fin normal-force coefficient, $\frac{N}{qS_f}$
$C_{Y_0}$	apparent center fin normal-force coefficient at $\beta = \delta_a = \delta_r = 0^\circ$
$C_{Y\beta}$	change in center fin normal-force coefficient with angle of sideslip, $\frac{\partial C_Y}{\partial \beta}$ , per deg
$C_{Y\delta_a}$	change in center fin normal-force coefficient with aileron deflection, $\frac{\partial C_Y}{\partial \delta_a}$ , per deg
$C_{Y\delta_r}$	change in center fin normal-force coefficient with rudder deflection, $\frac{\partial C_Y}{\partial \delta_r}$ , per deg
$c$	reference chord, m (ft)
$\bar{c}$	center fin reference mean aerodynamic chord, m (ft)
HM	hinge moment, m-N (ft-lb)
M	free-stream Mach number
N	center fin normal force, N (lb)
q	free-stream dynamic pressure, N/m <sup>2</sup> (lb/ft <sup>2</sup> )
S	reference area, m <sup>2</sup> (ft <sup>2</sup> )
T	center fin torsion, m-N (ft-lb)
$x_{cp}$	center fin chordwise center-of-pressure location, measured from leading edge of the reference mean aerodynamic chord, fraction of $\bar{c}$
$z_{cp}$	center fin spanwise center-of-pressure location, measured from the bending moment reference axis, fraction of b
$\alpha$	angle of attack, deg

$\beta$	angle of sideslip, deg
$\delta$	control surface deflection, deg
Subscripts:	
a	aileron, differential elevon
e	elevon
ef	elevon flap
f	center fin
if	inboard tip fin flap
of	outboard tip fin flap
r	rudder
sb	speed brake

## FLIGHT TEST VEHICLE

The HL-10 flight test vehicle (fig. 1(a)) is a low-aspect-ratio (1.156), wingless lifting body configuration incorporating a delta planform and negative camber with three stabilizing fins and four primary and six secondary control surfaces. A three-view drawing of the vehicle is shown in figure 1(b), and the pertinent physical characteristics are given in table 1.

The control surface pairs are located in the aft region of the vehicle. The split rudders are moved symmetrically outward as speed brakes or deflected in unison (i. e. , both rudders moved in the same direction) for yaw control. The two bulk elevons forming the rear portion of the lifting body are deflected symmetrically for pitch and longitudinal trim control and differentially for roll control. Two elevon flaps on the upper surface of the two elevons are deployed symmetrically to increase the base area. In addition, four tip fin flaps at the trailing edge of the tip fins are deflected to increase the base area.

Configurations A to D as defined by the positions of the speed brakes, elevon flaps, and the tip fin flaps are shown in the sketches of figure 2. All the flight test load data presented in this report, except the rudder hinge-moment coefficients, were acquired with the vehicle in configurations A and B, shown photographically in figures 3(a) and 3(b).

## FLIGHT TEST PROGRAM

The first 11 flight tests of the HL-10 vehicle were unpowered. Launch of the vehicle from a modified B-52 airplane at an altitude of 13,700 meters (45,000 feet) and

a Mach number of 0.65 to 0.75 was followed by a series of research maneuvers. The flights were concluded by gliding to a landing on Rogers dry lakebed. The second phase of the program consisted of a series of flights in which rocket power was used to expand the flight envelope to a maximum Mach number of approximately 1.85 and a peak altitude of approximately 27,400 meters (90,000 feet). Research maneuvers to investigate the subsonic, transonic, and supersonic flight characteristics of the vehicle were performed primarily during the rocket-engine-off portion of the flight. The subsonic flight data presented in this report were obtained at Mach numbers from 0.45 to 0.75, the transonic data at Mach numbers from 0.85 to 0.95, and the supersonic data at Mach numbers from 1.15 to 1.25. The vehicle angle of attack was varied from 5° to 30°, and the Reynolds number ranged from  $3.5 \times 10^6$  to  $62 \times 10^6$ , based on the vehicle length of 6.45 meters (21.17 feet).

## WIND-TUNNEL MODELS

Because of the evolutionary development of the HL-10 flight test configuration, various wind-tunnel tests were conducted with models which differed somewhat from the flight test vehicle. The major differences which may affect the loads data presented in this report are the shape of the tip fins and the geometry of the elevon and the elevon flap control surfaces. Early models did not incorporate the drooped leading edge on the tip fins (shown in fig. 2). The drooped leading edge was added to the flight test vehicle after the first flight to correct a flow separation problem. A more detailed description of the modification is given in reference 8.

The difference in the geometry of the elevon and elevon-flap control surfaces between the early small-scale models and the flight test vehicle is shown in figure 4. The major difference is in the planform of the elevon and elevon flap. The sides of the elevon and elevon flap on the flight vehicle are virtually parallel to the tip fin as shown in figure 4(a). The elevon and elevon flap of the small-scale model from reference 9 have outboard edges parallel to the vehicle centerline and inboard edges parallel to the tip fin as shown in figure 4(b); the elevon and elevon flap from reference 10 have both edges parallel to the vehicle centerline as shown in figure 4(c). The angle of the elevon flap deflection on the models also differs from that on the flight vehicle. The small-scale models and the associated test conditions are described more fully in references 9 and 10.

The full-scale wind-tunnel center fin loads and control surface hinge moments presented in this report were taken with the flight test vehicle in configurations C and D. The wind-tunnel test conditions are given in reference 12.

## INSTRUMENTATION

Ten strain gage bridges were installed in the root region of the three spars of the center fin shown in figure 5(a). The center fin gages were calibrated by using the point loading method discussed in reference 13.

Strain gage bridges were installed on the actuator mechanisms of the various control surfaces. These surfaces were calibrated in place on the vehicle.

During the flight tests the strain gage bridge outputs and other vehicle parameters were conditioned through the PCM system, telemetered to a ground station, and recorded on tape. The center fin and the control surface hinge-moment calibrations were used in a computer program to calculate the aerodynamic loads and load coefficients.

## METHOD OF ANALYSIS

The normal force, bending moment, and torsion acting on the center fin as shown in figures 5(a) and 5(b) are expressed in nondimensional form:

$$C_Y = \frac{N}{qS_f} \quad (1)$$

$$C_B = \frac{B}{qS_f b} \quad (2)$$

$$C_T = \frac{T}{qS_f \bar{c}} \quad (3)$$

The primary parameters affecting the center fin loads during a maneuver are angle of sideslip,  $\beta$ , aileron deflection,  $\delta_a$ , and rudder deflection,  $\delta_r$ . For small changes in these parameters, linear equations defining the effect of  $\beta$ ,  $\delta_a$ , and  $\delta_r$  on the center fin are:

$$C_Y = C_{Y_0} + C_{Y_\beta} \beta + C_{Y_{\delta_a}} \delta_a + C_{Y_{\delta_r}} \delta_r \quad (4)$$

$$C_T = C_{T_0} + C_{T_\beta} \beta + C_{T_{\delta_a}} \delta_a + C_{T_{\delta_r}} \delta_r \quad (5)$$

$$C_B = C_{B_0} + C_{B_\beta} \beta + C_{B_{\delta_a}} \delta_a + C_{B_{\delta_r}} \delta_r \quad (6)$$

The terms  $C_{Y_0}$ ,  $C_{T_0}$ , and  $C_{B_0}$  are apparent values included to allow for any asymmetries in the vehicle and any zero offsets in the data. The coefficients of the parameters in equations (4) to (6) are the slopes of the variations of the load coefficients with the respective parameters. To obtain these slopes the multiple regression models were applied, using a least-squares technique, to the aerodynamic load coeffi-

coefficients measured during lateral and longitudinal pulses and steady-state sideslips performed in the flight test program.

The validity of the preceding data reduction technique is illustrated by the time history in figure 6. The correlation between the measured values of the center fin normal-force coefficient and the values calculated from the linear regression model (eq. (4)) is shown. The variation in  $\beta$ ,  $\delta_r$ , and  $\delta_a$  during the flight test program was within the limits shown in figure 6.

The slopes of the center fin load coefficients defined by equations (4), (5), and (6) were used to calculate the center-of-pressure locations. The chordwise centers of pressure are referenced from the leading edge of the mean aerodynamic chord, and the spanwise centers of pressure are referenced from the bending-moment reference axis shown in figure 5(a).

The HL-10 control surface hinge moments are expressed in the following coefficient form:

Outboard tip fin flap

$$C_{h_{of}} = \frac{HM_{of}}{qS_{of}c_{of}} \quad (7)$$

Inboard tip fin flap

$$C_{h_{if}} = \frac{HM_{if}}{qS_{if}c_{if}} \quad (8)$$

Rudder

$$C_{h_r} = \frac{HM_r}{qS_r c_r} \quad (9)$$

Elevon flap

$$C_{h_{ef}} = \frac{HM_{ef}}{qS_{ef}c_{ef}} \quad (10)$$

Elevon

$$C_{h_e} = \frac{HM_e}{qS_e c_e} \quad (11)$$

The sign convention used is shown in figure 5(b). Because of the structural arrangement, the elevon hinge moment includes the load from the elevon flap.

The effects of angle of attack and elevon deflection on the elevon and elevon flap hinge moments were defined through the use of the same multiple regression technique.

These linear relationships are:

$$C_{he} = C_{he_o} + C_{he_\alpha} \alpha + C_{he_{\delta_e}} \delta_e \quad (12)$$

$$C_{hef} = C_{hef_o} + C_{hef_\alpha} \alpha + C_{hef_{\delta_e}} \delta_e \quad (13)$$

### ESTIMATED ERRORS

Flight aerodynamic load coefficient errors include the data acquisition system errors and the calibration errors. The control surface deflections and angle-of-sideslip errors are estimated from ground tests. Errors in angle of attack, dynamic pressure, and Mach number were obtained from reference 14.

The estimated errors for the vehicle parameters and aerodynamic load coefficients are summarized in the following table:

<u>Parameters</u>	<u>Error</u>
$\alpha$ , deg . . . . .	$\pm 0.5$
$\beta$ , deg . . . . .	$\pm 0.5$
$\delta_r$ , deg . . . . .	$\pm 0.85$
$\delta_e$ , deg . . . . .	$\pm 1.1$
$\delta_a$ , deg . . . . .	$\pm 1.5$
$\delta_{sb}$ , deg. . . . .	$\pm 0.85$
$q$ , N/m <sup>2</sup> (lb/ft <sup>2</sup> ) . . . . .	$\pm 96 (2)$
$M$ . . . . .	$\pm 0.01$
$C_Y$ . . . . .	$\pm 0.017$
$C_B$ . . . . .	$\pm 0.009$
$C_T$ . . . . .	$\pm 0.023$
$C_{h_{of}}$ . . . . .	$\pm 0.013$
$C_{h_{if}}$ . . . . .	$\pm 0.006$
$C_{h_r}$ . . . . .	$\pm 0.010$
$C_{hef}$ . . . . .	$\pm 0.010$
$C_{he}$ . . . . .	$\pm 0.010$

The error estimates for the quantities calculated from the multiple regression method are a measure of how well the regression models fit the flight data.

The estimated errors for the center fin normal-force-coefficient slopes and

associated centers of pressure are as follows:

$C_{Y\beta}$ . . . . .	$\pm 0.003$	$C_{Y\delta_r}$ . . . . .	$\pm 0.002$	$C_{Y\delta_a}$ . . . . .	$\pm 0.001$
$x_{cp}$ . . . . .	$\pm 0.06$	$x_{cp}$ . . . . .	$\pm 0.05$	$x_{cp}$ . . . . .	$\pm 0.05$
$z_{cp}$ . . . . .	$\pm 0.06$	$z_{cp}$ . . . . .	$\pm 0.06$	$z_{cp}$ . . . . .	$\pm 0.05$
					(M < 1.0)
					$\pm 0.14$
					(M > 1.0)

The errors for the elevon and elevon flap coefficient slopes are:

$C_{he\delta_e}$ . . . . .	$\pm 0.003$
$C_{hef\delta_e}$ . . . . .	$\pm 0.001$

## RESULTS AND DISCUSSION

### Center Fin Load Coefficient Slopes and Center-of-Pressure Locations

The flight test center fin normal-force-coefficient slopes and center-of-pressure locations are plotted versus angle of attack for subsonic, transonic, and supersonic Mach numbers in figures 7 to 9. The only comparable wind-tunnel center fin data are from the full-scale wind-tunnel tests at a Mach number of 0.25. These results are compared with equivalent flight test results in figures 8(a) and 9(a).

The variations of the normal-force coefficient slopes and center-of-pressure locations due to changes in angle of sideslip are shown in figures 7(a) to 7(c). In general, the normal-force-coefficient slope,  $C_{Y\beta}$ , remains constant with increasing angle of

attack for subsonic Mach numbers, decreases in magnitude for transonic and supersonic Mach numbers, but increases in magnitude with increasing Mach number for angles of attack less than 16°. The chordwise center-of-pressure location,  $x_{cp}$ , ranges from 0.10 to 0.30 for subsonic and transonic Mach numbers and increases to between 0.30 and 0.50 for supersonic Mach numbers. The spanwise center-of-pressure location,  $z_{cp}$ , remains between 0.40 and 0.60 at all Mach numbers and increases

slightly with increasing angle of attack at transonic and supersonic Mach numbers.

The variations of normal-force-coefficient slopes and center-of-pressure locations due to rudder deflection are shown in figures 8(a) to 8(c). As expected, the effect of rudder deflection on center fin normal-force coefficient is smaller at supersonic Mach numbers than at either subsonic or transonic Mach numbers. The chordwise center of pressure increases with increasing Mach number. The spanwise center of pressure

exhibits a slight shift outboard with increasing Mach number. Virtually no effect due to change in angle of attack was exhibited by these data. The full-scale wind-tunnel values (fig. 8(a)) agree well with the subsonic flight data.

Figure 9 shows that the normal-force-coefficient slopes due to aileron deflection remain constant for changes in angle of attack at subsonic and transonic Mach numbers but decrease in magnitude for supersonic Mach numbers. The chordwise center of pressure shows no change with angle of attack and only a slight increase from subsonic to transonic Mach numbers (figs. 9(a) and 9(b)). For supersonic Mach numbers (fig. 9(c)) the data are insufficient to establish any trends. The spanwise center of pressure shows no change due to variations in angle of attack or Mach number at subsonic and transonic Mach numbers. For supersonic Mach numbers, it is farther outboard but moves inboard with increasing angle of attack. The full-scale wind-tunnel values (fig. 9(a)) agree well with the subsonic flight data at  $16^\circ$  angle of attack.

The center fin normal-force-coefficient slopes and center-of-pressure locations due to sideslip, rudder deflection, and aileron deflection shown in figures 7(a), 8(a), and 9(a) were not affected by differences between flight configurations A and B nor by the differences between wind-tunnel configurations C and D.

#### Control Surface Hinge-Moment Coefficients

The flight test and wind-tunnel test control surface hinge-moment coefficients are plotted against angle of attack for subsonic, transonic, and supersonic Mach numbers in figures 10 to 14.

The outboard tip fin flap hinge-moment coefficient,  $C_{h_{of}}$ , is shown in figures 10(a) to 10(c). In general,  $C_{h_{of}}$  increases slightly with increasing angle of attack at subsonic and supersonic Mach numbers and remains constant at transonic Mach numbers. Subsonically, it increases primarily with the tip fin flap deflections from the closed configurations A and C to the open configurations B and D. The only comparable wind-tunnel data are from the full-scale wind-tunnel tests at Mach 0.25. These data show excellent agreement with the flight data (fig. 10(a)) for both the closed and open tip fin flap positions.

The flight test and wind-tunnel inboard tip fin flap hinge-moment coefficients are plotted against angle of attack in figures 11(a) to 11(c). In general, the flight and full-scale wind-tunnel values remain essentially constant for changes in angle of attack at subsonic and transonic Mach numbers. The flight values decrease with increasing angle of attack at supersonic Mach numbers. The small-scale wind-tunnel data (ref. 9) indicate some variations with angle of attack not shown by the flight data. Subsonically (fig. 11(a)), the flight test values are slightly larger in magnitude than either the full-scale or the small-scale wind-tunnel values and increase primarily with tip fin flap deflections. At transonic and supersonic Mach numbers the flight test data in general show fair agreement with the small-scale wind-tunnel values.

Figures 12(a) to 12(c) are plots of the rudder hinge-moment coefficient,  $C_{h_r}$ , against angle of attack at several speed brake deflections. Subsonically,  $C_{h_r}$  remains

constant for changes in angle of attack. At transonic and supersonic Mach numbers it in general increases slightly with increasing angle of attack. The magnitude of  $C_{h_r}$  due to speed brake deflection increases with increasing Mach number at all angles of attack investigated. The only comparable wind-tunnel data are from the full-scale wind-tunnel test at Mach 0.25. In general, the flight and wind-tunnel data agreed well (fig. 12(a)).

The elevon flap hinge-moment coefficient,  $C_{h_{ef}}$ , is shown as a function of angle of attack in figure 13. In general,  $C_{h_{ef}}$  decreases with increasing angle of attack and at subsonic speeds increases with increasing elevon flap deflection. The slope due to angle of attack becomes more negative with increasing Mach number. Even though the elevon flap deflection angle of the wind-tunnel models was slightly different from that of the flight vehicle (fig. 4), the small-scale and the full-scale wind-tunnel data show good agreement with the flight data.

The elevon hinge-moment coefficient,  $C_{h_e}$ , versus angle of attack is shown in figures 14(a) to 14(c). Subsonically,  $C_{h_e}$  increases with increasing elevon flap deflection. The elevon hinge-moment coefficient decreases with increasing angle of attack and its variation with angle of attack becomes more negative with an increase in Mach number. Both the small-scale and the full-scale wind-tunnel values are slightly higher than the flight values.

The elevon hinge-moment-coefficient slope due to elevon deflection is plotted versus angle of attack in figures 15(a) to 15(c). In general, the flight test values remain constant for changes in angle of attack but show an increase from -0.013 to -0.027 through the Mach number range. At subsonic Mach numbers (fig. 15(a)) the slope is not affected by change in configuration. The small-scale wind-tunnel data are lower in magnitude than the flight test values and are sensitive to changes in angle of attack especially at supersonic speeds (fig. 15(c)).

The effect of Mach number on the control surface hinge-moment coefficients at constant angle of attack is shown in figure 16. The outboard tip fin flap, rudder, and elevon flap hinge-moment coefficients all show the expected increase in magnitude at transonic and low supersonic Mach numbers. In general, the inboard tip fin flap and elevon hinge-moment coefficients decrease with increasing Mach number. The full-scale wind-tunnel values of  $C_{h_{of}}$ ,  $C_{h_r}$ ,  $C_{h_{ef}}$ , and  $C_{h_e}$  at Mach 0.25 agree well with the extrapolated flight test values. However, both the full-scale and the small-scale wind-tunnel values of  $C_{h_{if}}$  are lower than the flight results for Mach numbers less than 1.1. The small-scale wind-tunnel  $C_{h_{ef}}$  data show good agreement with the flight test results. The small-scale  $C_{h_e}$  data are generally higher in magnitude than the flight test results.

Because of the proximity of the control surfaces to the rocket engine, changes in the hinge-moment coefficients were evident during rocket engine operation (36,696 N (8250 lb) thrust). This change is shown in figure 17. With the exception of

the elevon, all control surface hinge-moment coefficients showed a marked decrease in magnitude during the rocket engine operation. The outboard and inboard tip fin flap hinge-moment coefficients showed a more pronounced engine effect at the lower angles of attack. The engine effect on the rudder and elevon flap hinge-moment coefficients,  $C_{h_r}$  and  $C_{h_{ef}}$ , remained nearly constant at all angles of attack. The decrease in

hinge moment was caused by the increase in base pressure during rocket engine operation which increased the pressure on the inner sides of the control surfaces and hence reduced the magnitudes of the hinge moments. Although figure 17 shows the engine power effect at Mach 1.2, the decrease in hinge moment first became apparent at Mach 1.0.

### CONCLUDING REMARKS

Center fin loads and control surface hinge moments obtained during the HL-10 lifting body flight test program were compared with available wind-tunnel predictions. The center fin normal-force coefficients and center-of-pressure locations were primarily affected by angle of sideslip, rudder deflection, and aileron deflection and secondarily by angle of attack and Mach number. The limited amount of full-scale wind-tunnel center fin data showed good agreement with the flight test center fin loads.

The outboard and inboard tip fin flap hinge-moment coefficients increased primarily with tip fin flap deflection from the closed to the open configurations. The rudder hinge-moment coefficient increased with increasing speed brake deflection. This effect was more pronounced at the higher Mach numbers. The elevon flap and elevon hinge-moment coefficients increased with elevon flap deflection and decreased with increasing angle of attack.

The outboard tip fin flap, rudder, and elevon flap hinge-moment coefficients showed the expected increase in magnitude at transonic and low supersonic Mach numbers.

With the exception of the elevon, all control surface hinge-moment coefficients showed a marked decrease in magnitude during rocket engine operation.

Despite differences between the wind-tunnel models and the flight test vehicle, in general the wind-tunnel values adequately predicted the aerodynamic loads experienced in the HL-10 flight test program.

Flight Research Center,  
National Aeronautics and Space Administration,  
Edwards, Calif., August 20, 1971.

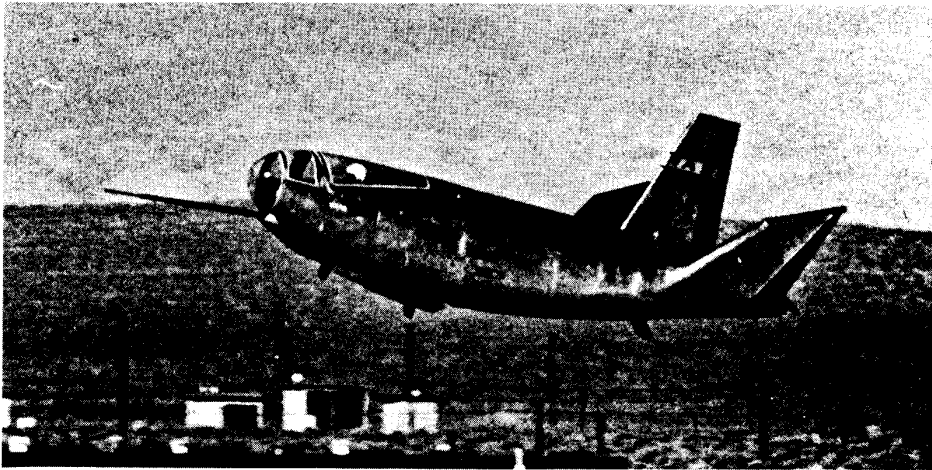
## REFERENCES

1. Tang, Ming H. : Correlation of Flight-Test Loads With Wind-Tunnel Predicted Loads on Three Lifting Body Vehicles. Flight-Test Results Pertaining to the Space Shuttlecraft. NASA TM X-2101, 1970.
2. Jenkins, Jerald M. ; Tang, Ming H. ; and Pearson, George P. E. : Vertical-Tail Loads and Control-Surface Hinge-Moment Measurements on the M2-F2 Lifting Body During Initial Subsonic Flight Tests. NASA TM X-1712, 1968.
3. Tang, Ming H. ; and DeAngelis, V. Michael: Fin Loads and Control-Surface Hinge Moments Measured in Full-Scale Wind-Tunnel Tests on the X-24A Flight Vehicle. NASA TM X-1922, 1969.
4. Rainey, Robert W. ; and Ladson, Charles L. : Aerodynamic Characteristics of a Manned Lifting Entry Vehicle at Mach Numbers From 0.2 to 1.2. NASA TM X-1015, 1964.
5. Campbell, James F. ; and Jernell, Lloyd S. : Effects of Various Center-Fin and Tip-Fin Arrangements on Aerodynamic Characteristics of a Manned Lifting Entry Vehicle From Mach Numbers 1.50 to 2.86. NASA TM X-1299, 1966.
6. Spencer, Bernard, Jr. : Effects of Elevon Planform on Low-Speed Aerodynamic Characteristics of the HL-10 Manned Lifting Entry Vehicle. NASA TM X-1409, 1967.
7. Rainey, Robert W. : Summary of an Advanced Manned Lifting Entry Vehicle Study. NASA TM X-1159, 1965.
8. McKinney, Linwood W. ; and Huffman, Jarrett K. : Subsonic Aerodynamic Characteristics of a Model of the HL-10 Flight Research Vehicle With Basic and Modified Tip Fins. NASA TM X-2119, 1971.
9. Harris, Charles D. : Control-Surface Hinge-Moment and Elevon Normal-Force Characteristics at Transonic Speeds on a Manned Lifting Entry Vehicle. NASA TM X-1241, 1966.
10. Campbell, James F. ; and Grow, Josephine W. : Stability and Control Characteristics of a Manned Lifting Entry Vehicle at Mach Numbers From 1.50 to 2.16 Including Hinge Moment and Pressure Distribution Data. NASA TM X-1314, 1966.
11. Mechtly, E. A. : The International System of Units - Physical Constants and Conversion Factors. NASA SP-7012, 1969.
12. Gamse, Berl; and Mort, Kenneth W. : Full-Scale Wind-Tunnel Investigation of the HL-10 Manned Lifting Body Flight Vehicle. NASA TM X-1476, 1967.

13. Skopinski, T. H. ; Aiken, William S. , Jr. ; and Houston, Wilber B. : Calibration of Strain-Gage Installations in Aircraft Structures for the Measurement of Flight Loads. NACA Rept. 1178, 1954.
14. Pyle, Jon S. : Lift and Drag Characteristics of the HL-10 Lifting Body During Subsonic Gliding Flight. NASA TN D-6263, 1971.

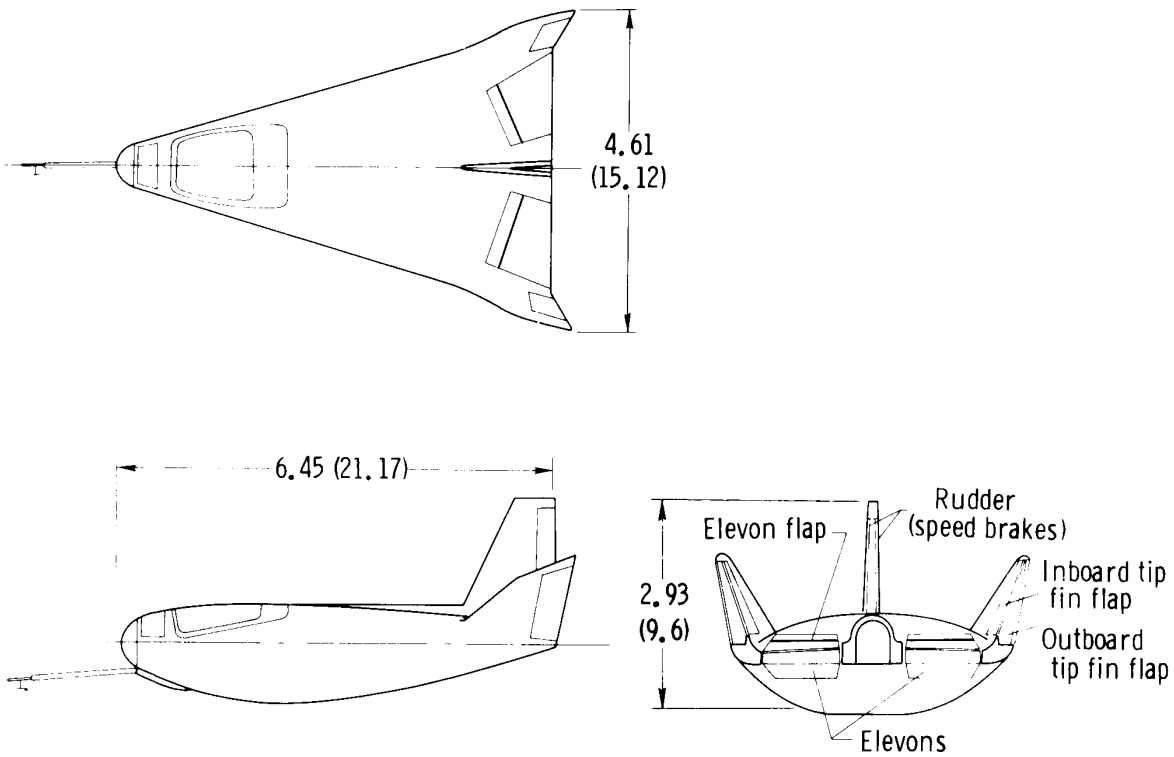
TABLE 1. PHYSICAL CHARACTERISTICS OF THE HL-10 VEHICLE

Body -	
Reference planform area, m <sup>2</sup> (ft <sup>2</sup> ) . . . . .	14.9 (160)
Length, m (ft) . . . . .	6.45 (21.17)
Span, m (ft) . . . . .	4.15 (13.6)
Aspect ratio (basic vehicle), $\frac{b^2}{S}$ . . . . .	1.156
Weight, including pilot, N (lb) . . . . .	26,690 (6000)
Center of gravity, percentage of reference length . . . . .	51.8
Elevons (two) -	
Area, each, m <sup>2</sup> (ft <sup>2</sup> ) . . . . .	1.00 (10.72)
Reference area, m <sup>2</sup> (ft <sup>2</sup> ) . . . . .	0.82 (8.89)
Span, parallel to hinge line, m (ft) . . . . .	1.09 (3.58)
Chord, perpendicular to hinge line:	
Root, m (ft) . . . . .	0.59 (1.93)
Tip, m (ft) . . . . .	1.24 (4.06)
Reference chord, m (ft) . . . . .	0.76 (2.48)
Elevon flaps (two) -	
Area, each, m <sup>2</sup> (ft <sup>2</sup> ) . . . . .	0.70 (7.50)
Span, each, parallel to hinge line, m (ft) . . . . .	1.09 (3.58)
Chord, perpendicular to hinge line:	
Root, m (ft) . . . . .	0.48 (1.58)
Tip, m (ft) . . . . .	0.80 (2.63)
Reference chord, m (ft) . . . . .	0.64 (2.09)
Vertical stabilizer -	
Area, m <sup>2</sup> (ft <sup>2</sup> ) . . . . .	1.47 (15.8)
Reference area, m <sup>2</sup> (ft <sup>2</sup> ) . . . . .	1.38 (14.85)
Reference span, m (ft) . . . . .	1.48 (4.84)
Height, trailing edge, m (ft) . . . . .	1.53 (5.02)
Chord:	
Root, m (ft) . . . . .	1.32 (4.32)
Tip, m (ft) . . . . .	0.60 (1.97)
Reference mean aerodynamic chord, m (ft) . . . . .	0.98 (3.23)
Leading-edge sweep, deg . . . . .	25
Rudders (two) -	
Area, each, m <sup>2</sup> (ft <sup>2</sup> ) . . . . .	0.41 (4.45)
Height, each, m (ft) . . . . .	1.26 (4.12)
Chord, m (ft) . . . . .	0.33 (1.08)
Outboard tip fin flaps (two) -	
Area, each, m <sup>2</sup> (ft <sup>2</sup> ) . . . . .	0.35 (3.77)
Height, hinge line, m (ft) . . . . .	1.37 (4.50)
Chord, perpendicular to hinge line, m (ft) . . . . .	0.26 (0.84)
Inboard tip fin flaps (two) -	
Area, each, m <sup>2</sup> (ft <sup>2</sup> ) . . . . .	0.23 (2.48)
Height, hinge line, m (ft) . . . . .	1.01 (3.31)
Chord, perpendicular to hinge line, m (ft) . . . . .	0.23 (0.75)



E-16207

(a) Flight test vehicle.



(b) Three-view drawing. Dimensions in meters (feet).

Figure 1. HL-10 lifting body vehicle.

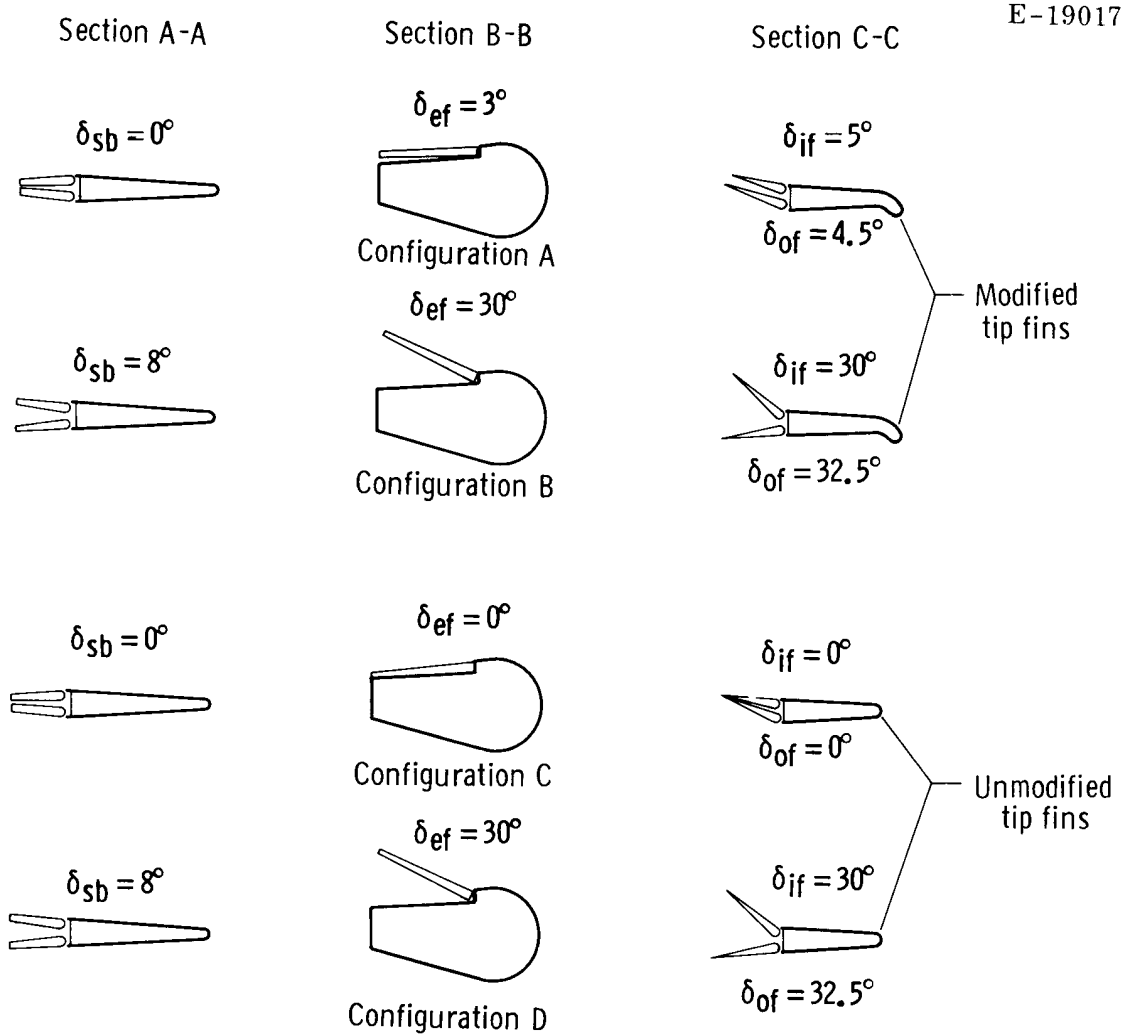
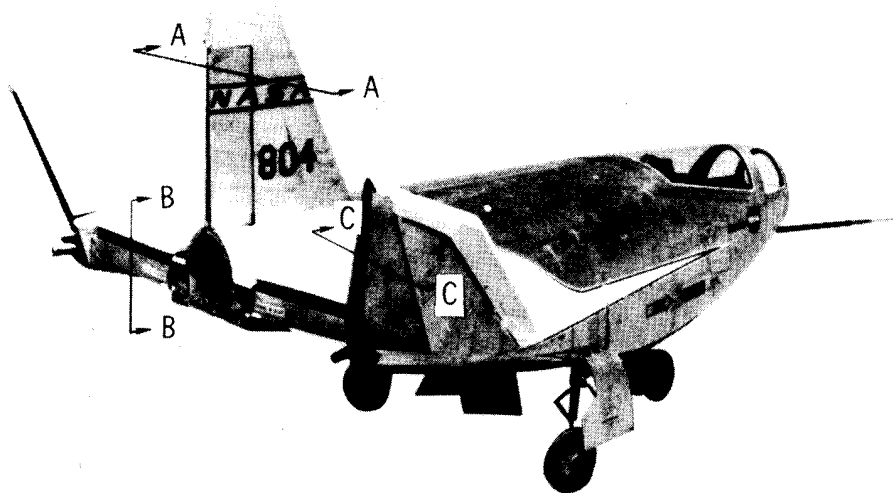
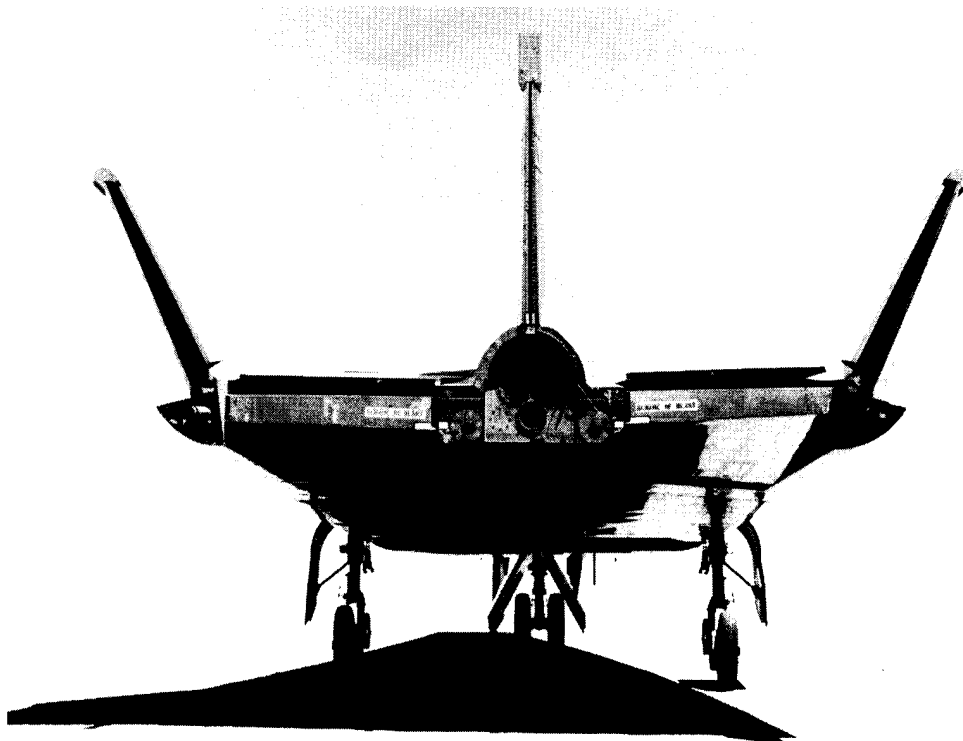
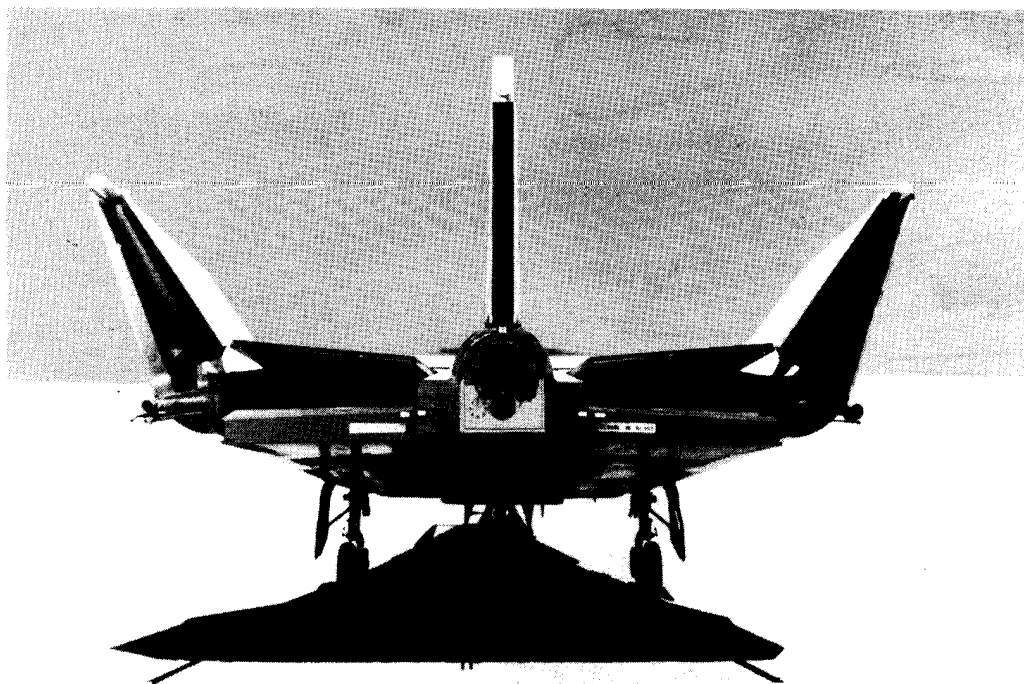


Figure 2. HL-10 configurations A to D defined by the speed brake, elevon flap, and tip fin flap positions.

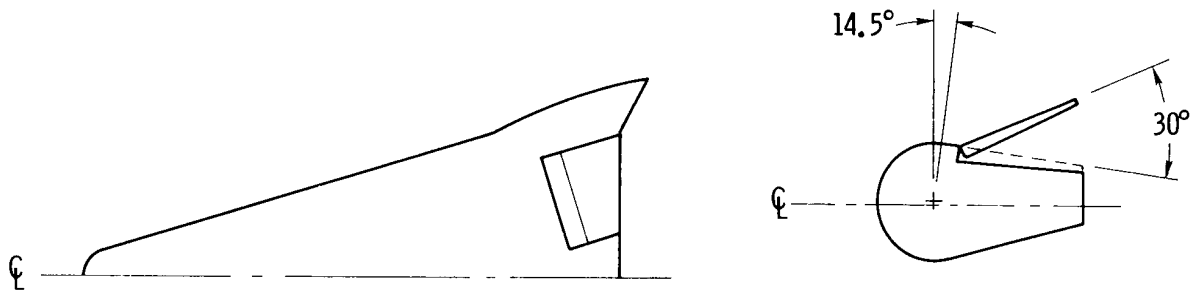


(a) Configuration A.

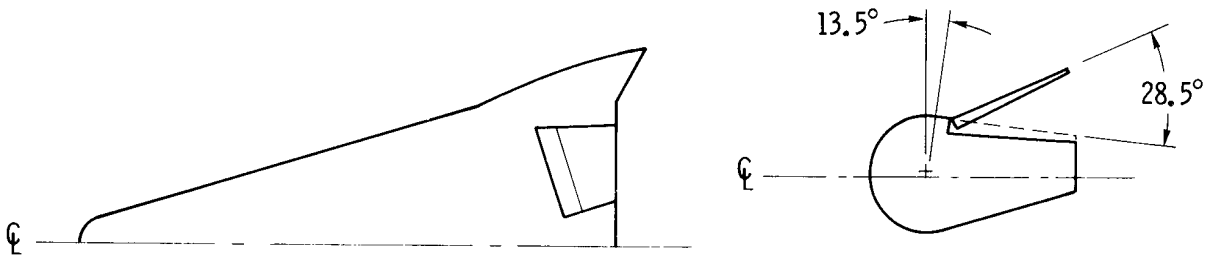


(b) Configuration B.

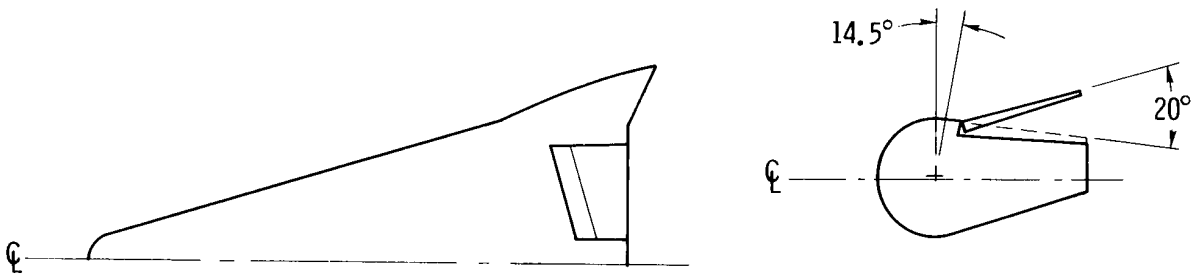
Figure 3. Rear view of HL-10 lifting-body research vehicle.



(a) Flight vehicle.

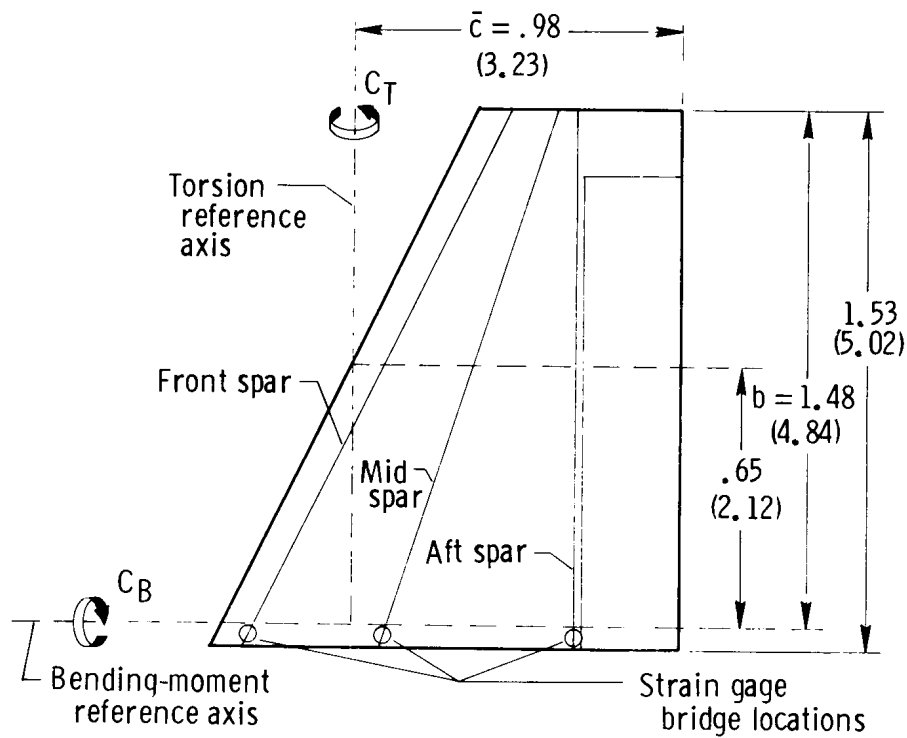


(b) Small-scale wind-tunnel model (ref. 9).

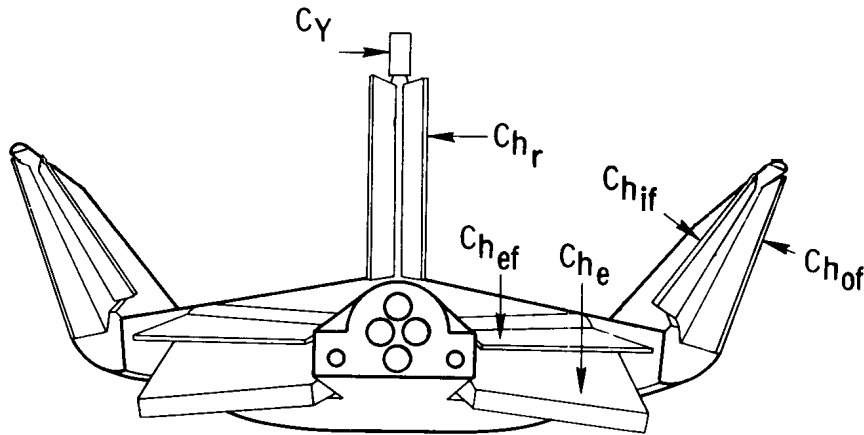


(c) Small-scale wind-tunnel model (ref. 10).

Figure 4. HL-10 elevon planform and cross section views.



(a) Center fin. Dimensions in meters (feet).



(b) Center fin and control surfaces.

Figure 5. Strain-gage locations on the center fin and sign conventions of center fin loads and control surface hinge-moment measurements for the HL-10 lifting body vehicle. Arrows indicate direction of positive load and hinge moments.

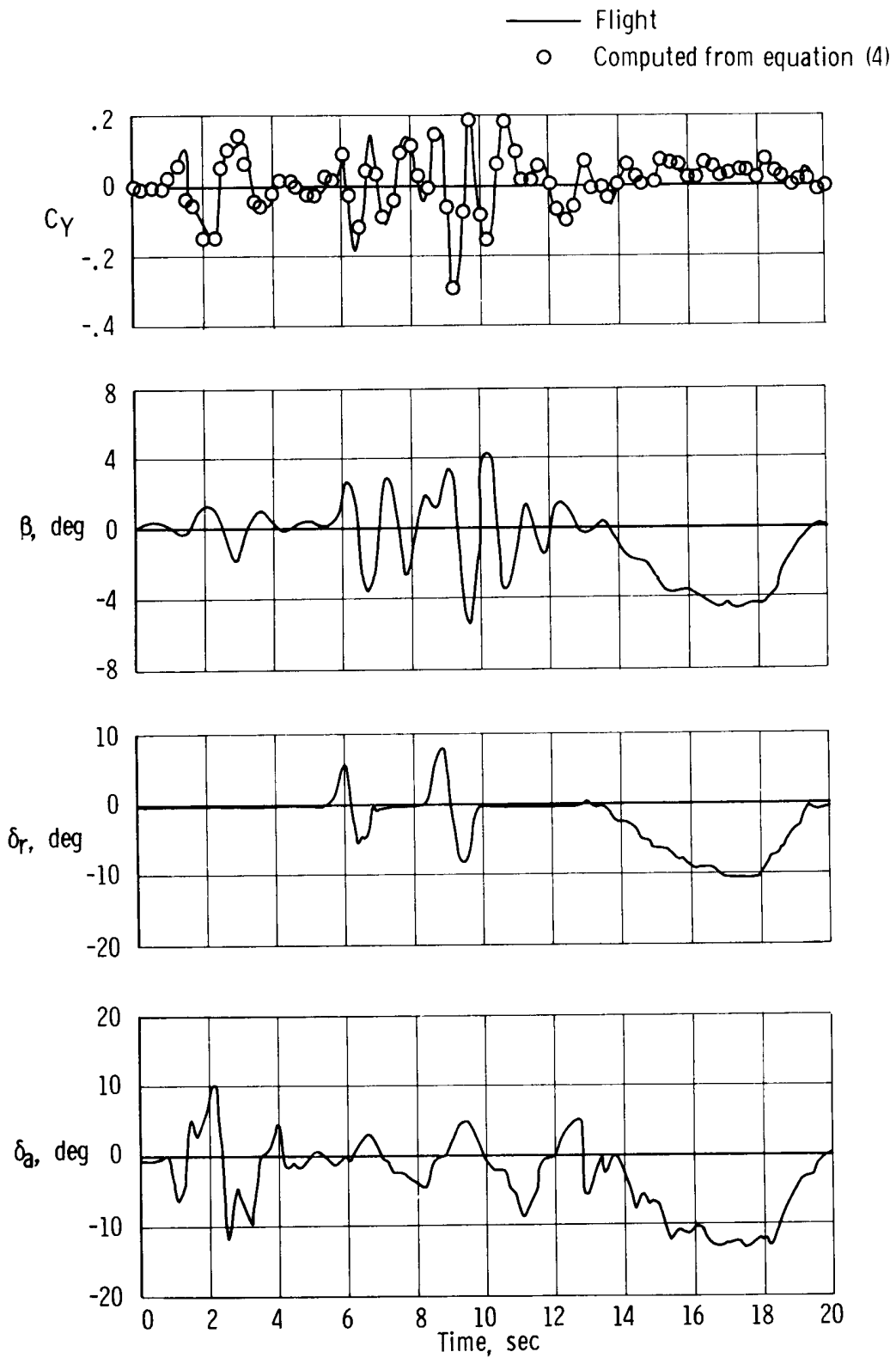
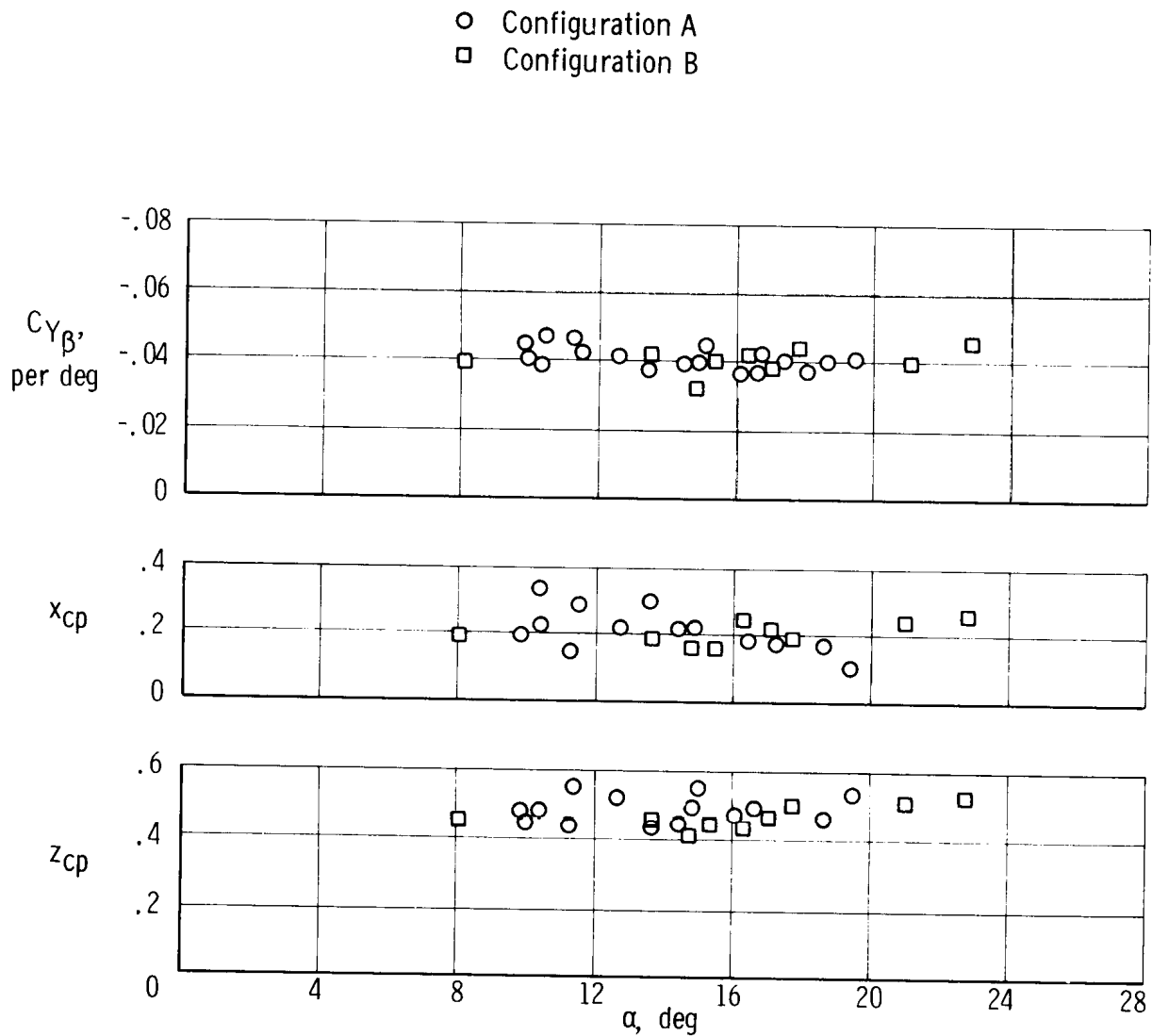
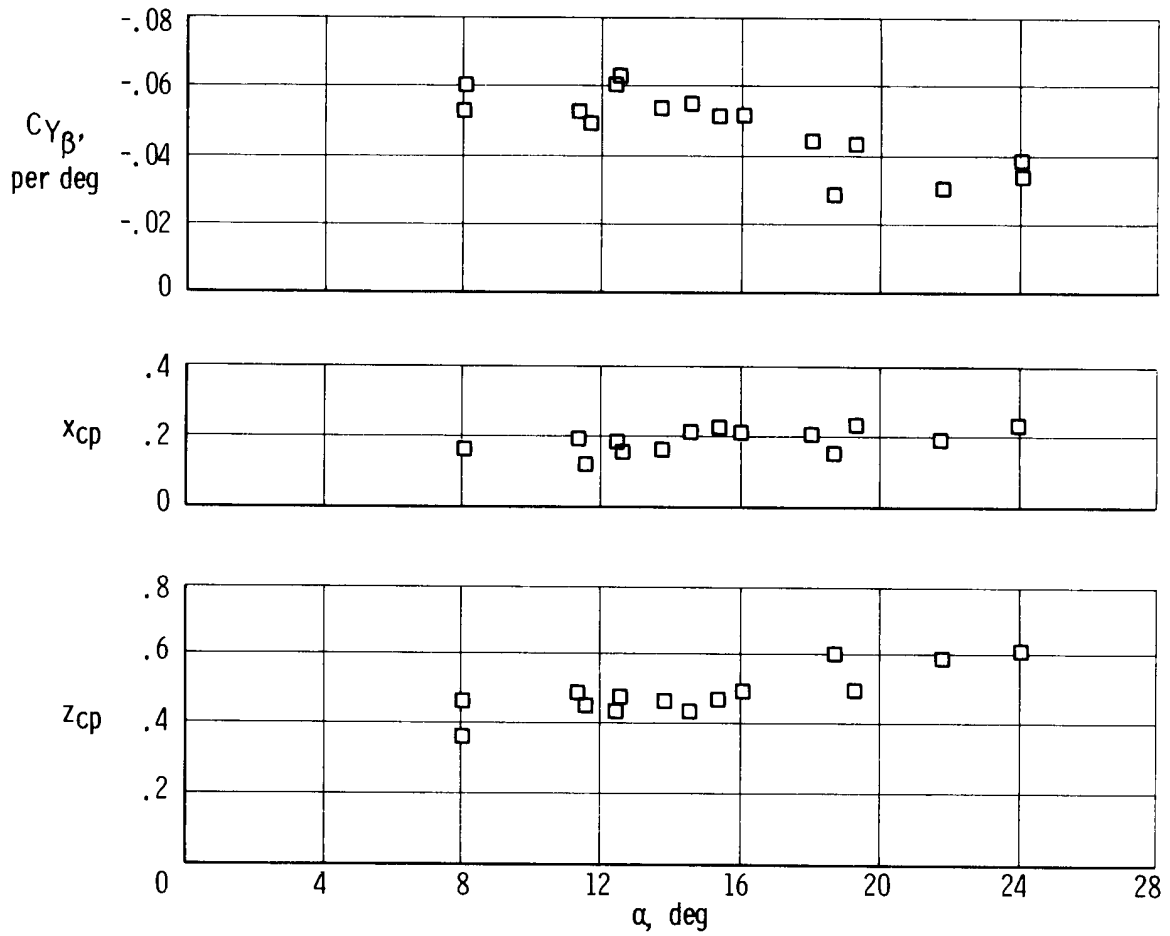


Figure 6. HL-10 flight maneuver time history.  $\alpha = 11.4^\circ$  to  $15.6^\circ$ ;  $M = 0.72$  to  $0.74$ ;  $q = 8570$  to  $10,917$  N/m<sup>2</sup> (179 to 228 lb/ft<sup>2</sup>); configuration B.



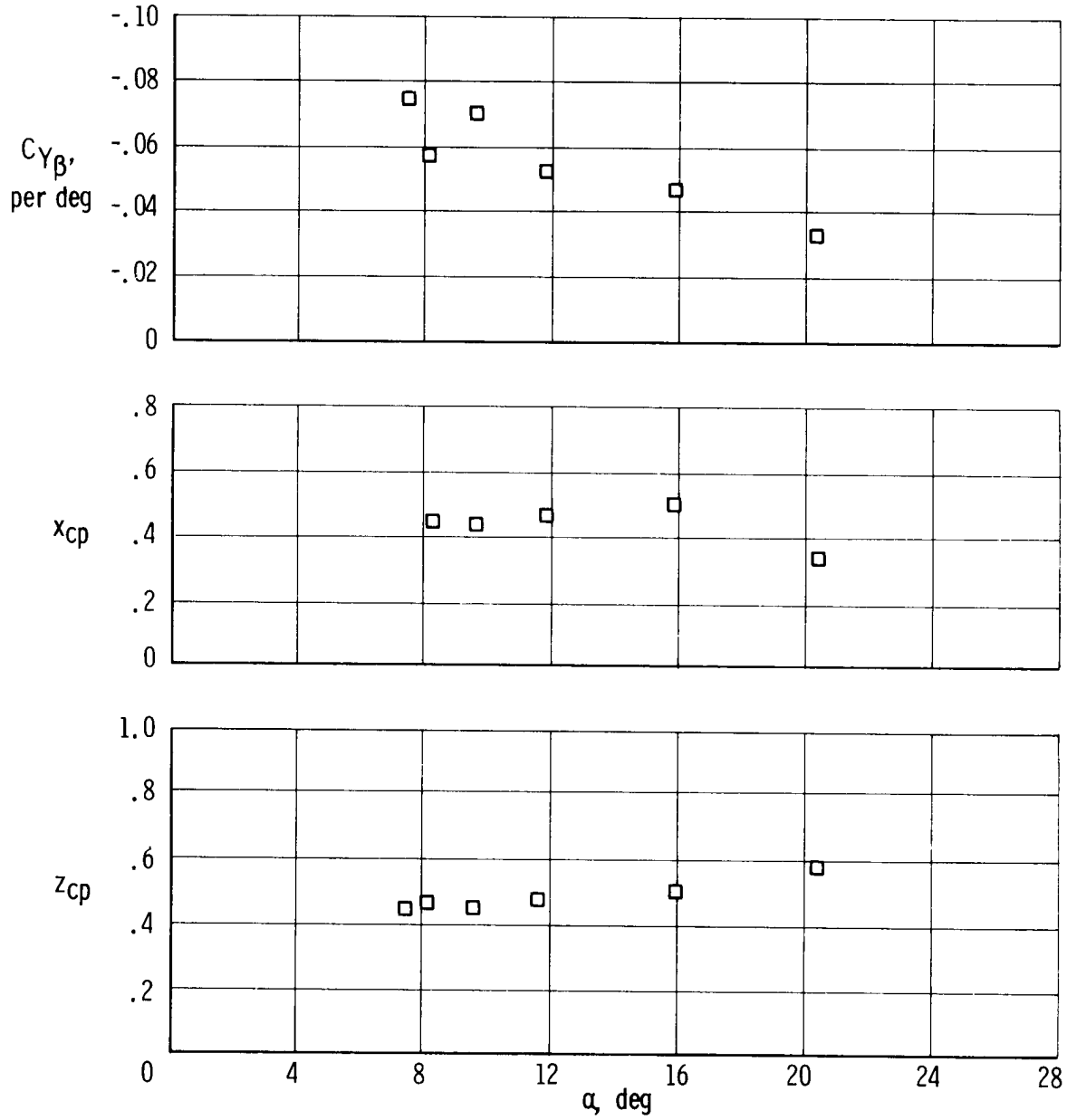
(a)  $M = 0.45$  to  $0.75$ .

Figure 7. Flight-measured center fin normal-force-coefficient slope and center-of-pressure locations due to change in angle of sideslip as a function of angle of attack.



(b)  $M = 0.85$  to  $0.95$ ; configuration B.

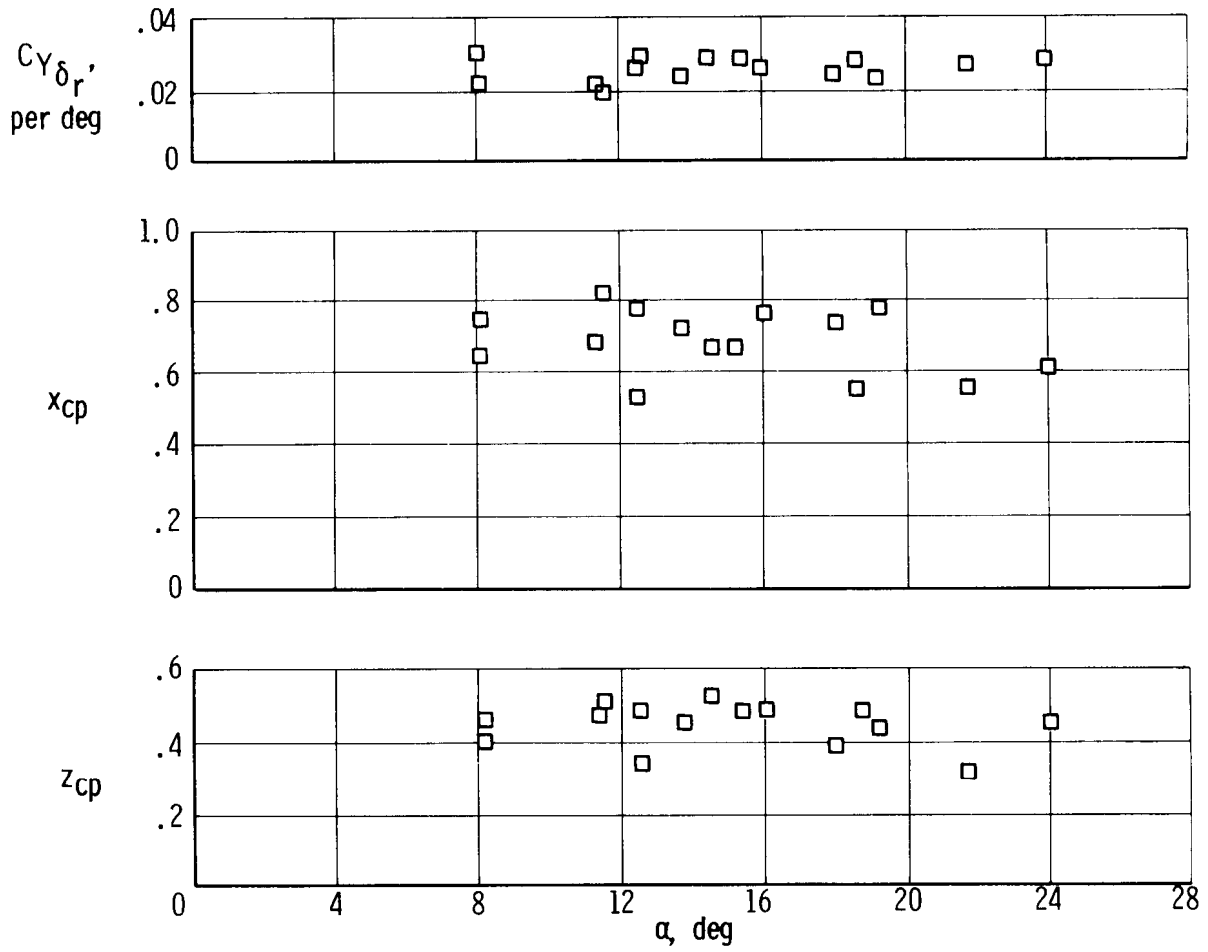
Figure 7. Continued.



(c)  $M = 1.15$  to  $1.25$ ; configuration B.

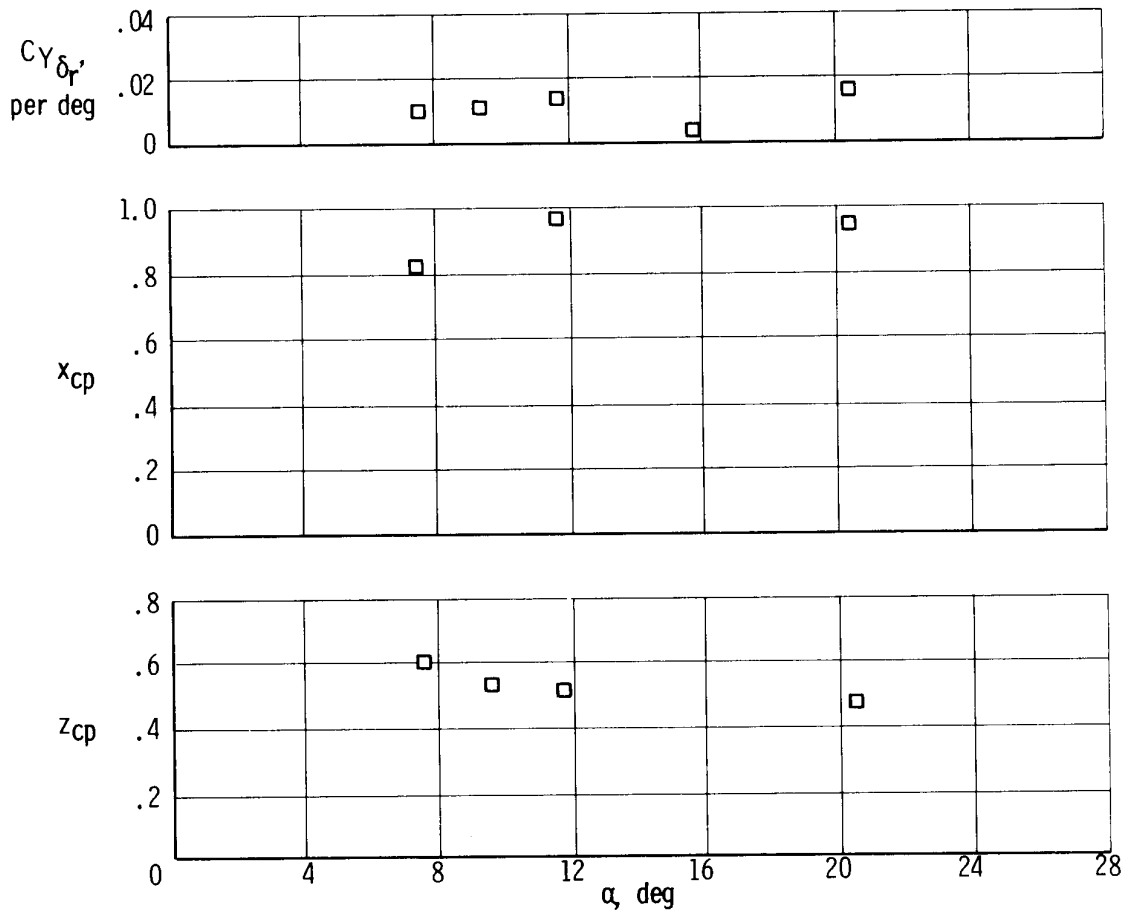
Figure 7. Concluded.





(b)  $M = 0.85$  to  $0.95$ ; flight configuration B.

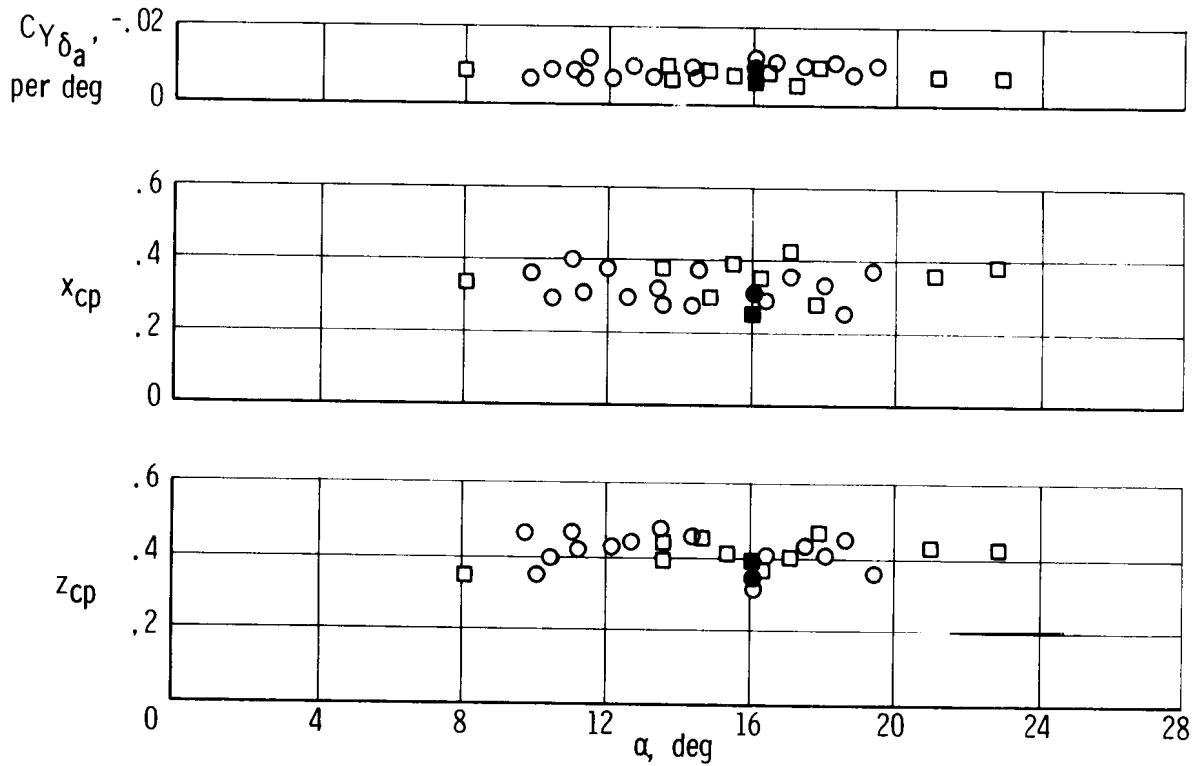
Figure 8. Continued.



(c)  $M = 1.15$  to  $1.25$ ; flight configuration B.

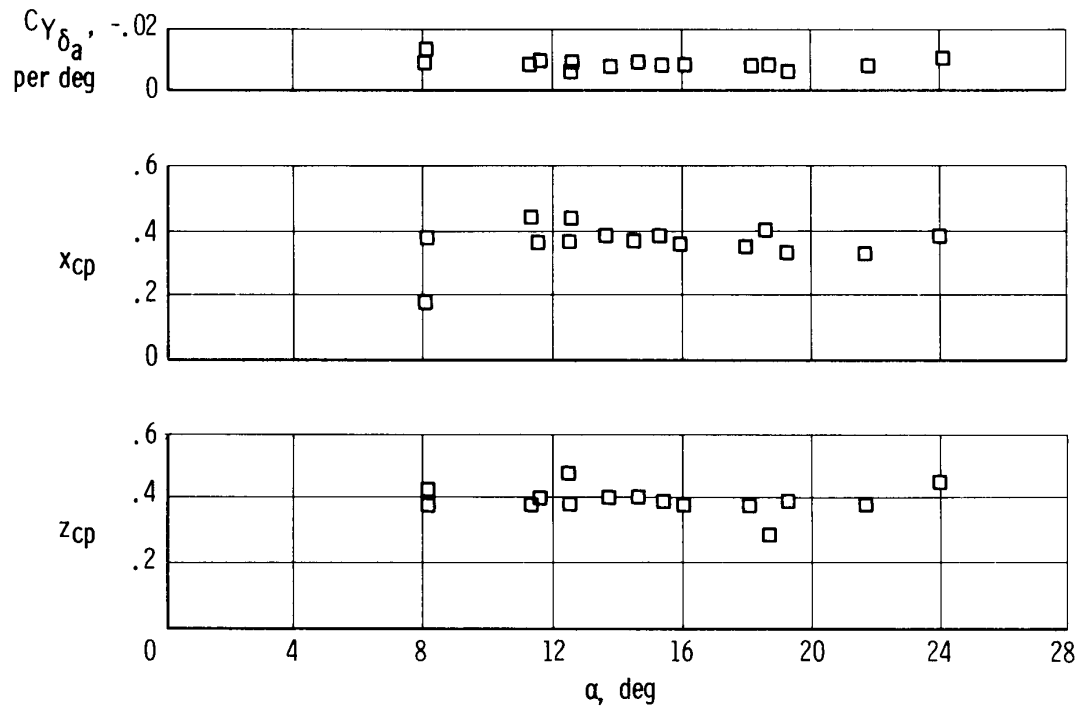
Figure 8. Concluded.

- Configuration A } Flight,  $M = 0.45$  to  $0.75$
- Configuration B } Flight,  $M = 0.45$  to  $0.75$
- Configuration C } Full-scale wind tunnel,  $M = 0.25$
- Configuration D } Full-scale wind tunnel,  $M = 0.25$



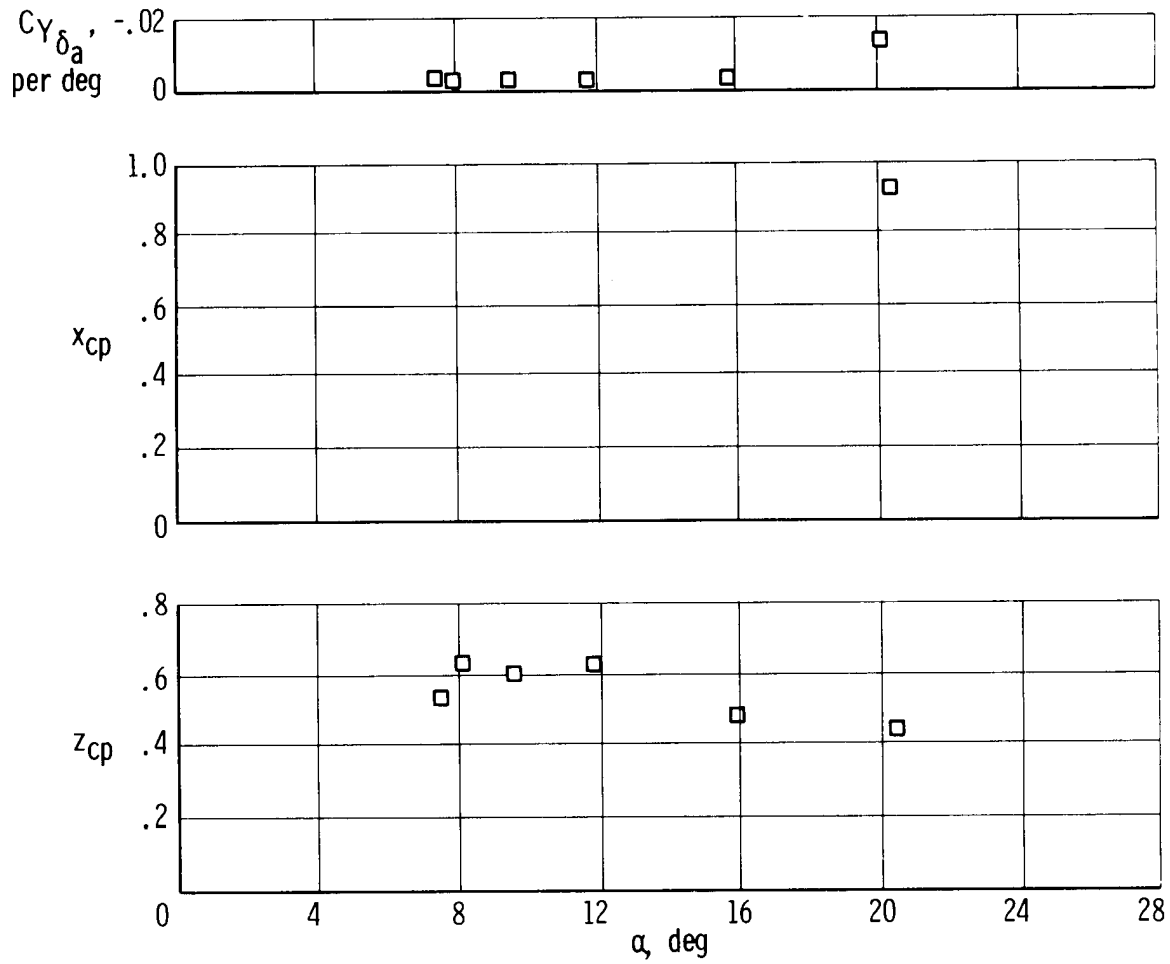
(a)  $M = 0.25$  to  $0.75$ .

Figure 9. Center fin normal-force-coefficient slope and center-of-pressure locations due to aileron deflection as a function of angle of attack.



(b)  $M = 0.85$  to  $0.95$ ; flight configuration B.

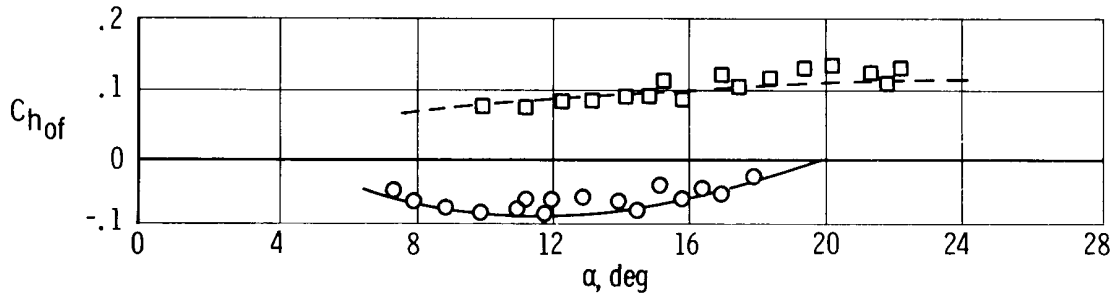
Figure 9. Continued.



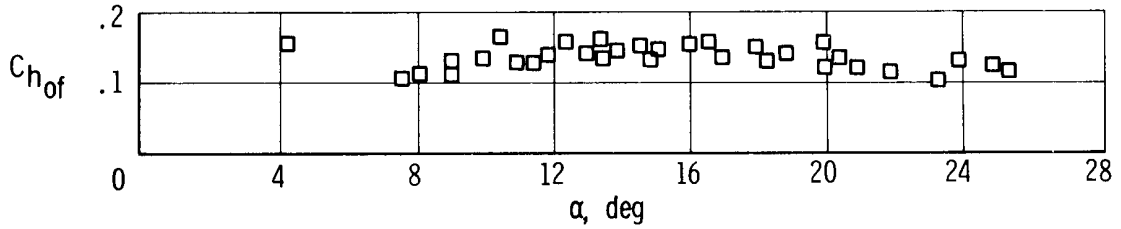
(c)  $M = 1.15$  to  $1.25$ ; flight configuration B.

Figure 9. Concluded.

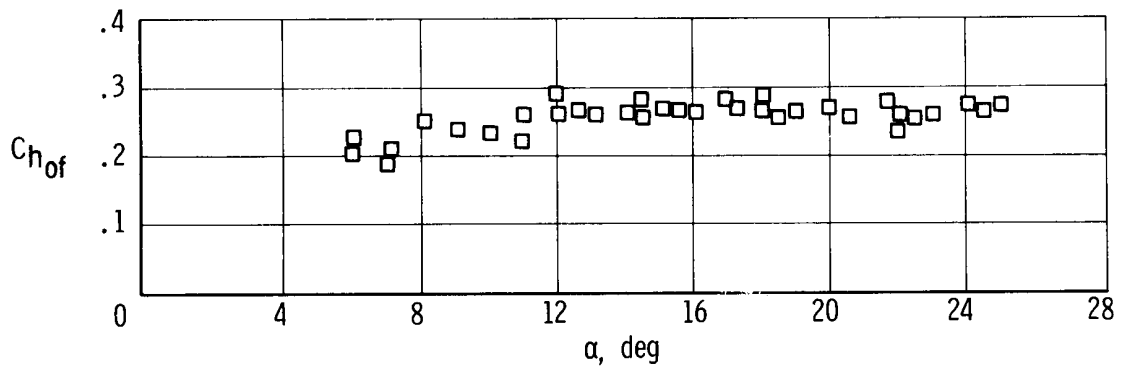
○ Configuration A } Flight  
 □ Configuration B }  
 — Configuration C } Full-scale wind tunnel, M = 0.25  
 - - - Configuration D }



(a)  $M = 0.25$  to  $0.63$ .



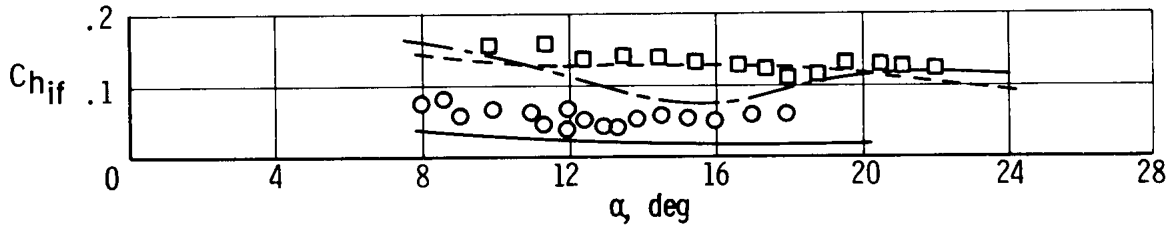
(b)  $M = 0.87$  to  $0.93$ .



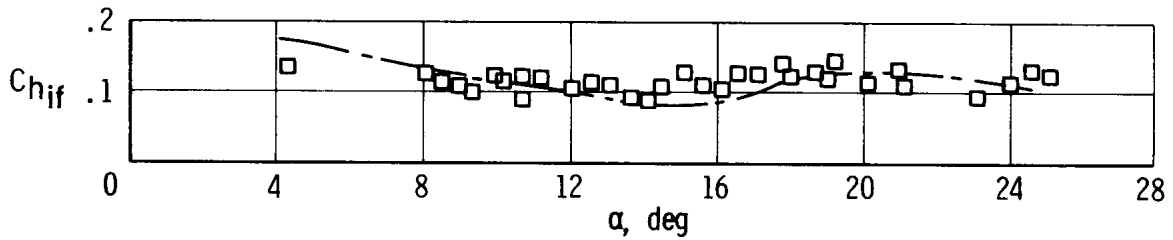
(c)  $M = 1.17$  to  $1.23$ .

Figure 10. Comparison of the flight outboard tip fin flap hinge-moment coefficients with wind-tunnel predicted values.  $\beta = 0^\circ$ ;  $\delta_r = 0^\circ$ ;  $\delta_a = 0^\circ$ ;  $\delta_e = -11^\circ$  to  $11^\circ$ .

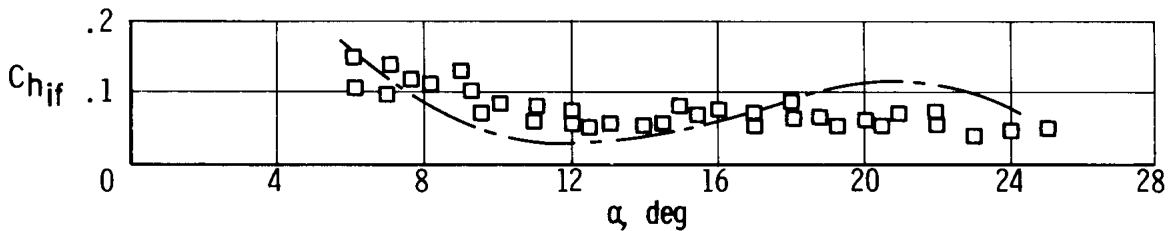
- Configuration A } Flight
- Configuration B } Flight
- Configuration C } Full-scale wind tunnel, M = 0.25
- - - Configuration D } Full-scale wind tunnel, M = 0.25
- · - Configuration D, reference 9, M = 0.60, 0.80, 1.20



(a)  $M = 0.25$  to  $0.63$ .

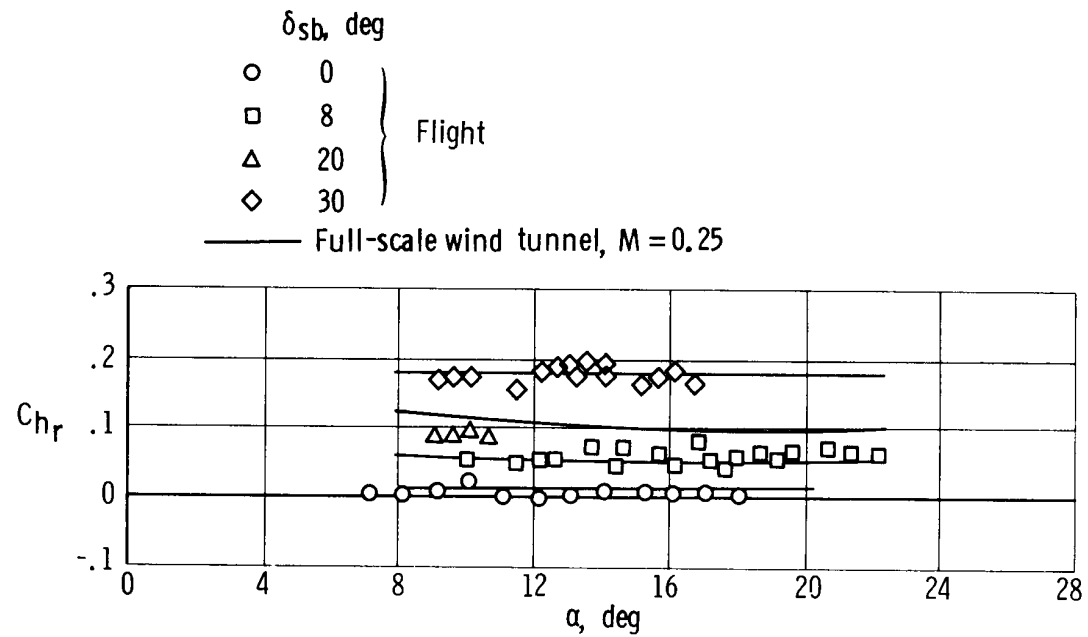


(b)  $M = 0.80$  to  $0.93$ .

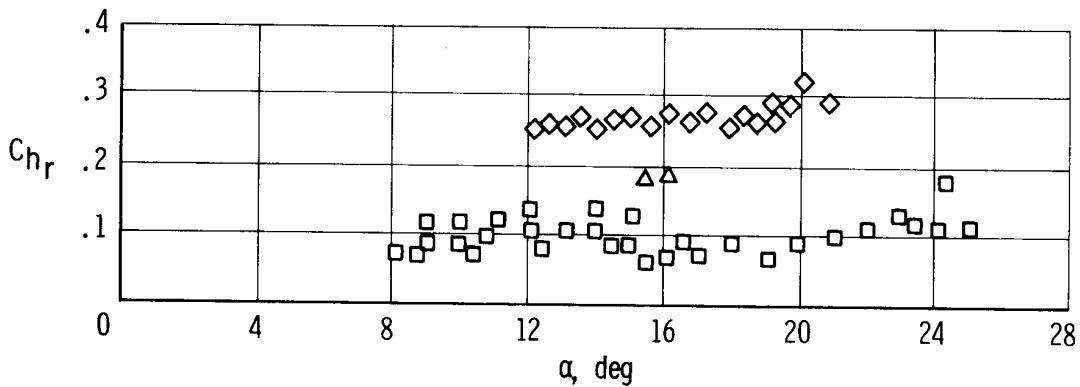


(c)  $M = 1.17$  to  $1.23$ .

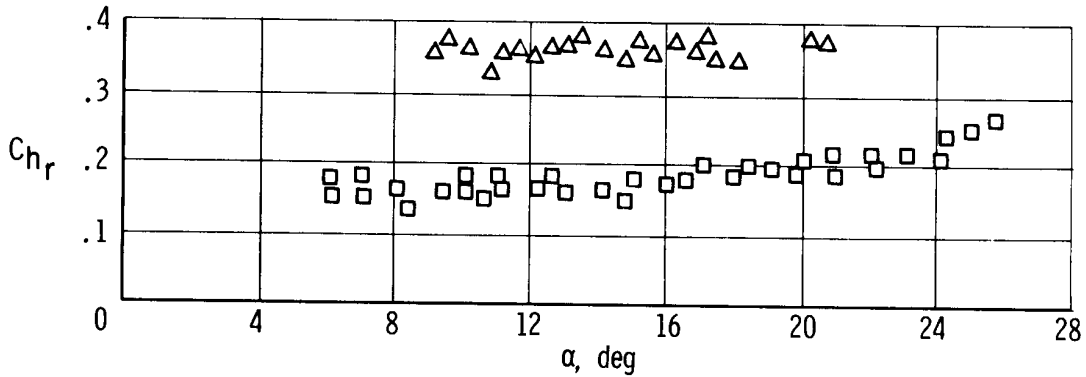
Figure 11. Comparison of the flight inboard tip fin flap hinge-moment coefficients with wind-tunnel predicted values.  $\beta = 0^\circ$ ;  $\delta_r = 0^\circ$ ;  $\delta_a = 0^\circ$ ;  $\delta_e = -11^\circ$  to  $11^\circ$ .



(a)  $M = 0.25$  to  $0.63$ .



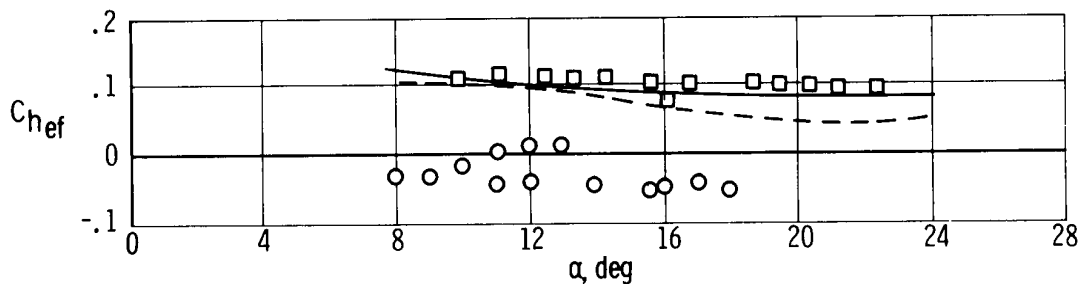
(b)  $M = 0.87$  to  $0.93$ .



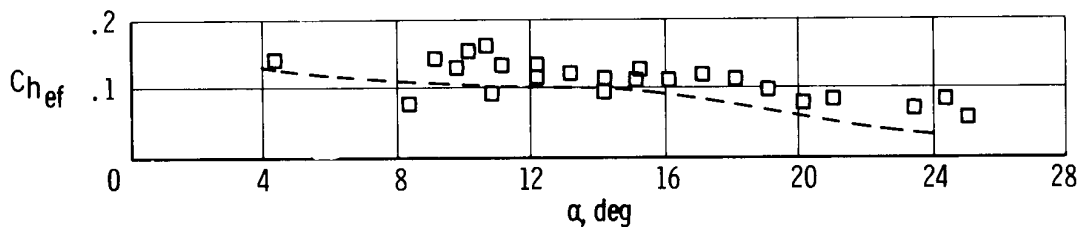
(c)  $M = 1.17$  to  $1.23$ .

Figure 12. Comparison of the flight rudder hinge-moment coefficients with wind-tunnel predicted values.  $\beta = 0^\circ$ ;  $\delta_r = 0^\circ$ ;  $\delta_a = 0^\circ$ ;  $\delta_e = -11^\circ$  to  $11^\circ$ .

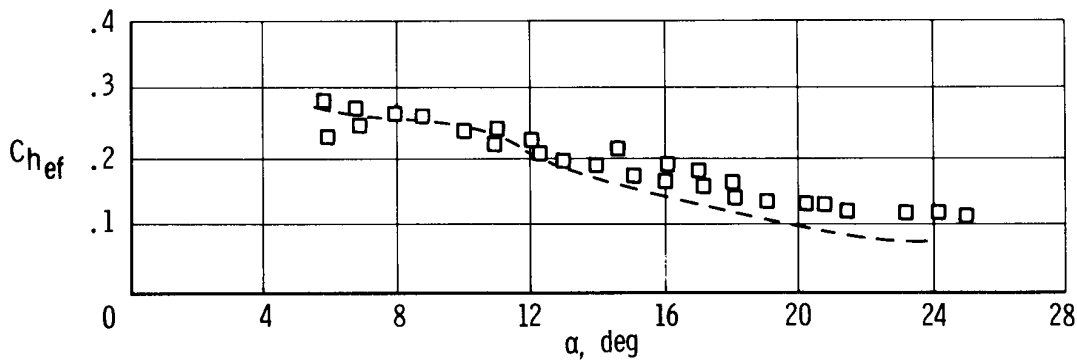
- Configuration A } Flight
- Configuration B } Flight
- Configuration D, full-scale wind tunnel,  $M = 0.25$
- - - Configuration D, reference 9,  $M = 0.60, 0.80, 1.20$



(a)  $M = 0.25$  to  $0.63$ .

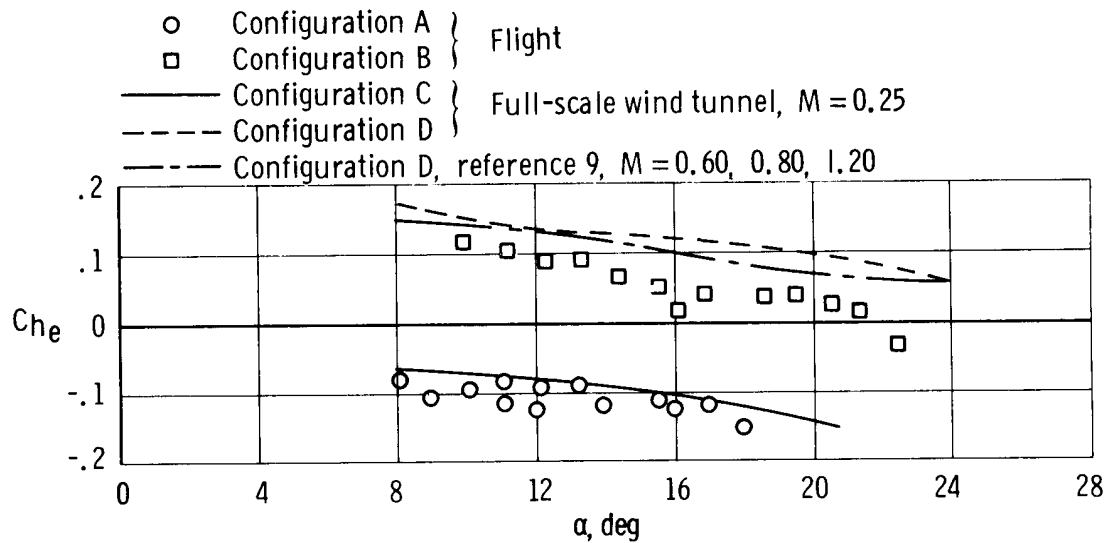


(b)  $M = 0.80$  to  $0.93$ .

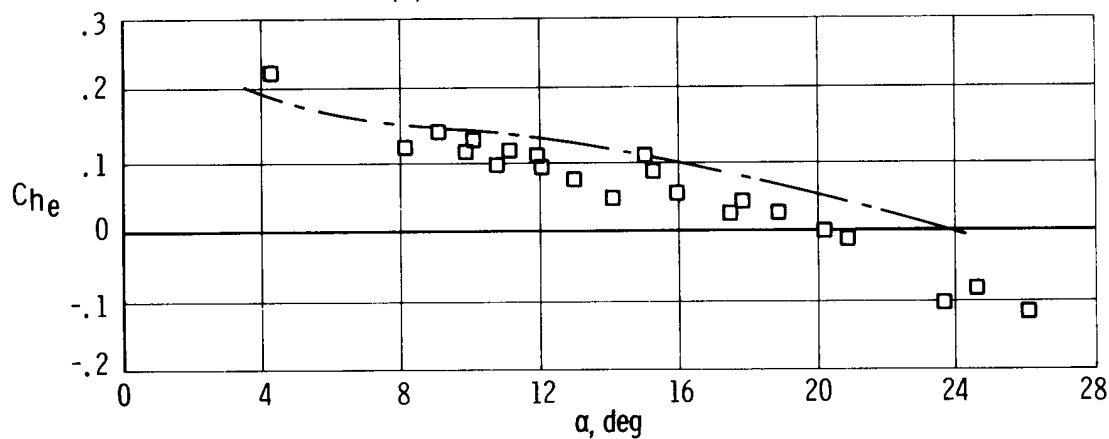


(c)  $M = 1.17$  to  $1.23$ .

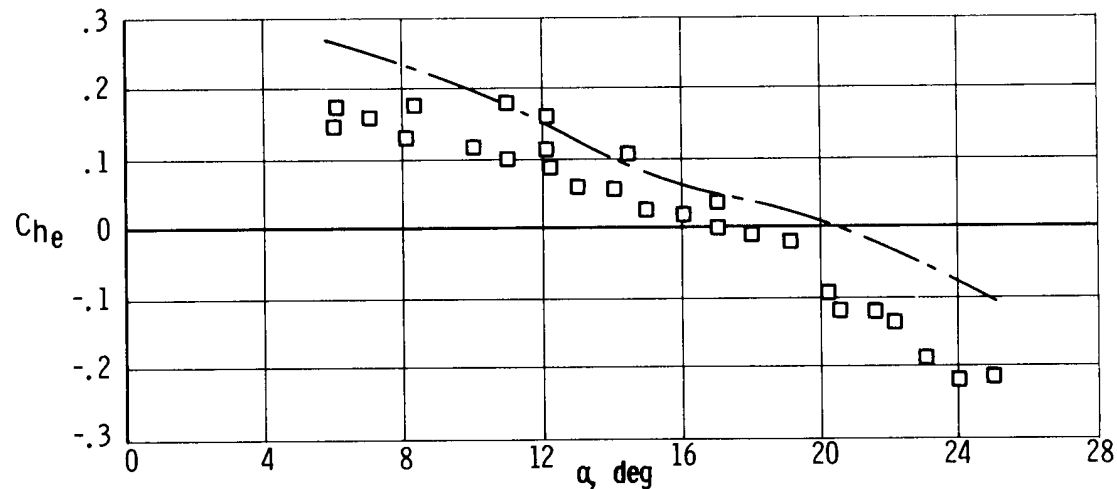
Figure 13. Comparison of the flight elevon flap hinge-moment coefficients with wind-tunnel predicted values.  $\beta = 0^\circ$ ;  $\delta_r = 0^\circ$ ;  $\delta_a = 0^\circ$ ;  $\delta_e$  corrected to  $0^\circ$ .



(a)  $M = 0.25$  to  $0.63$ .



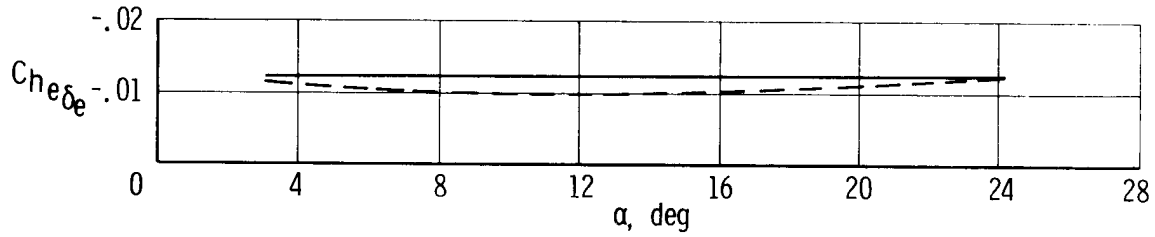
(b)  $M = 0.80$  to  $0.93$ .



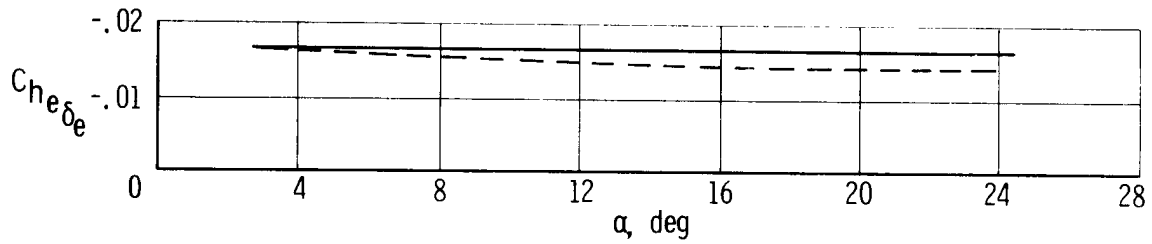
(c)  $M = 1.17$  to  $1.23$ .

Figure 14. Comparison of the flight elevon hinge-moment coefficients with wind-tunnel predicted values.  $\beta = 0^\circ$ ;  $\delta_r = 0^\circ$ ;  $\delta_a = 0^\circ$ ;  $\delta_e$  corrected to  $0^\circ$ .

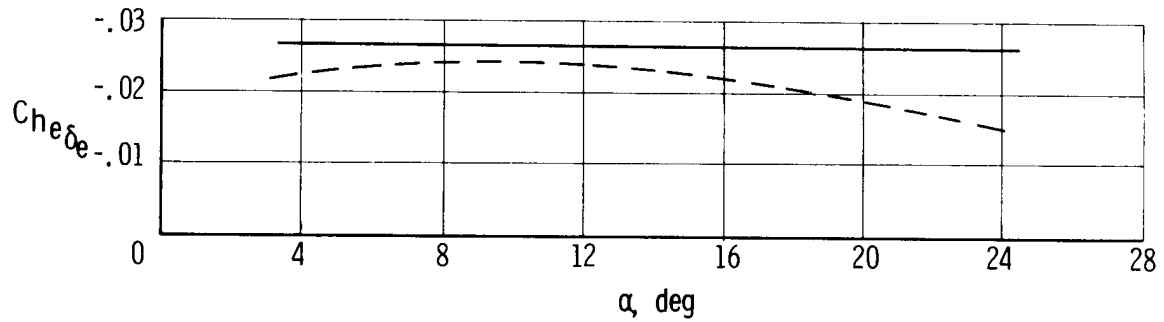
— Configurations A and B, flight  
 - - - Configuration D, reference 9, M = 0.60, 0.80, 1.20



(a)  $M = 0.45$  to  $0.75$ .



(b)  $M = 0.80$  to  $0.95$ .



(c)  $M = 1.15$  to  $1.25$ .

Figure 15. Comparison of the flight elevon hinge-moment coefficient slope due to elevon deflection with wind-tunnel predicted values.

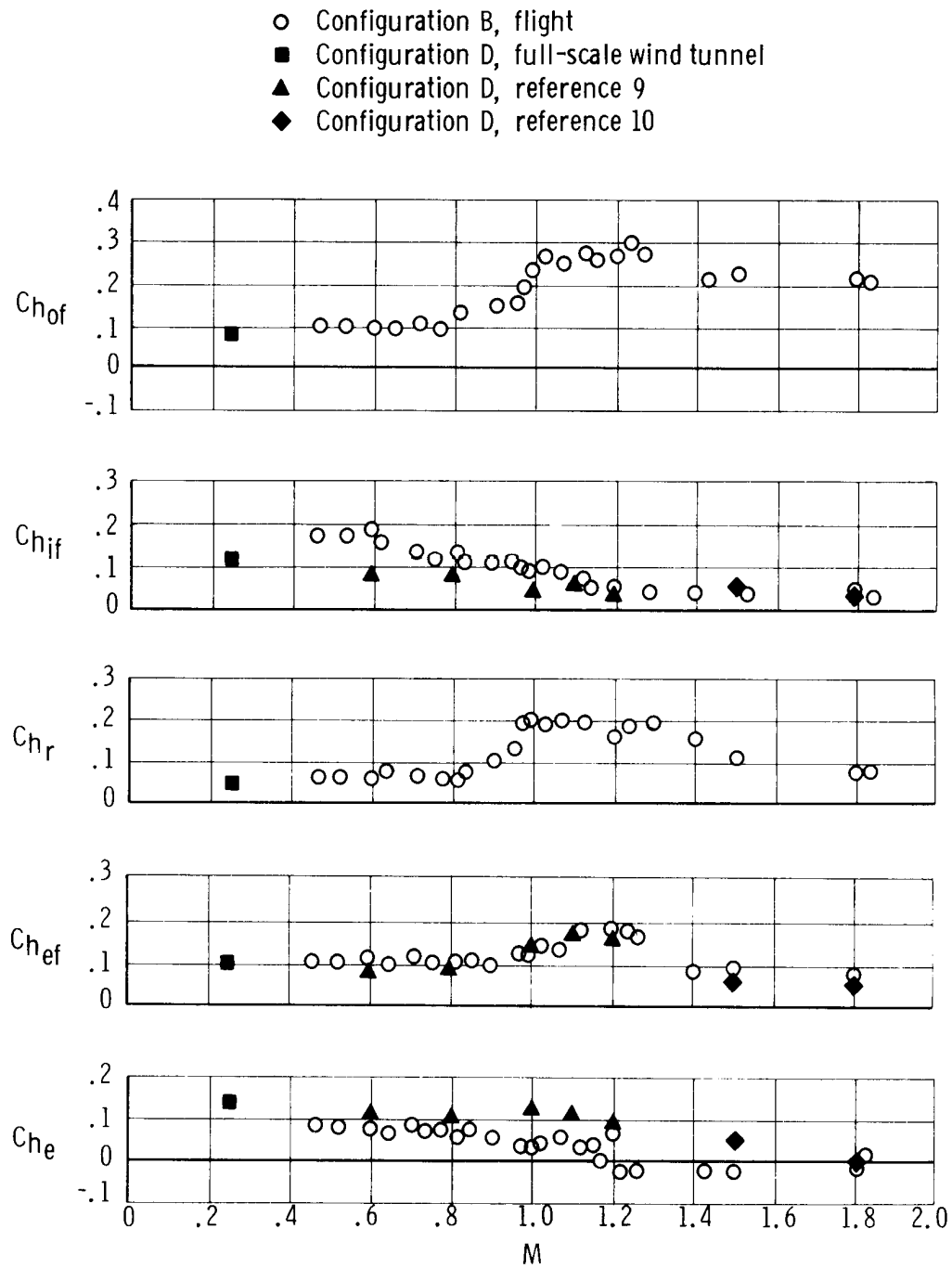


Figure 16. Comparison of the flight control surface hinge-moment-coefficient variation with Mach number with wind-tunnel predicted values.  $\alpha = 14^\circ$ ;  $\beta = 0^\circ$ ;  $\delta_a = 0^\circ$ ;  $\delta_r = 0^\circ$ . (Control surface deflections shown in figures 2 and 4.)

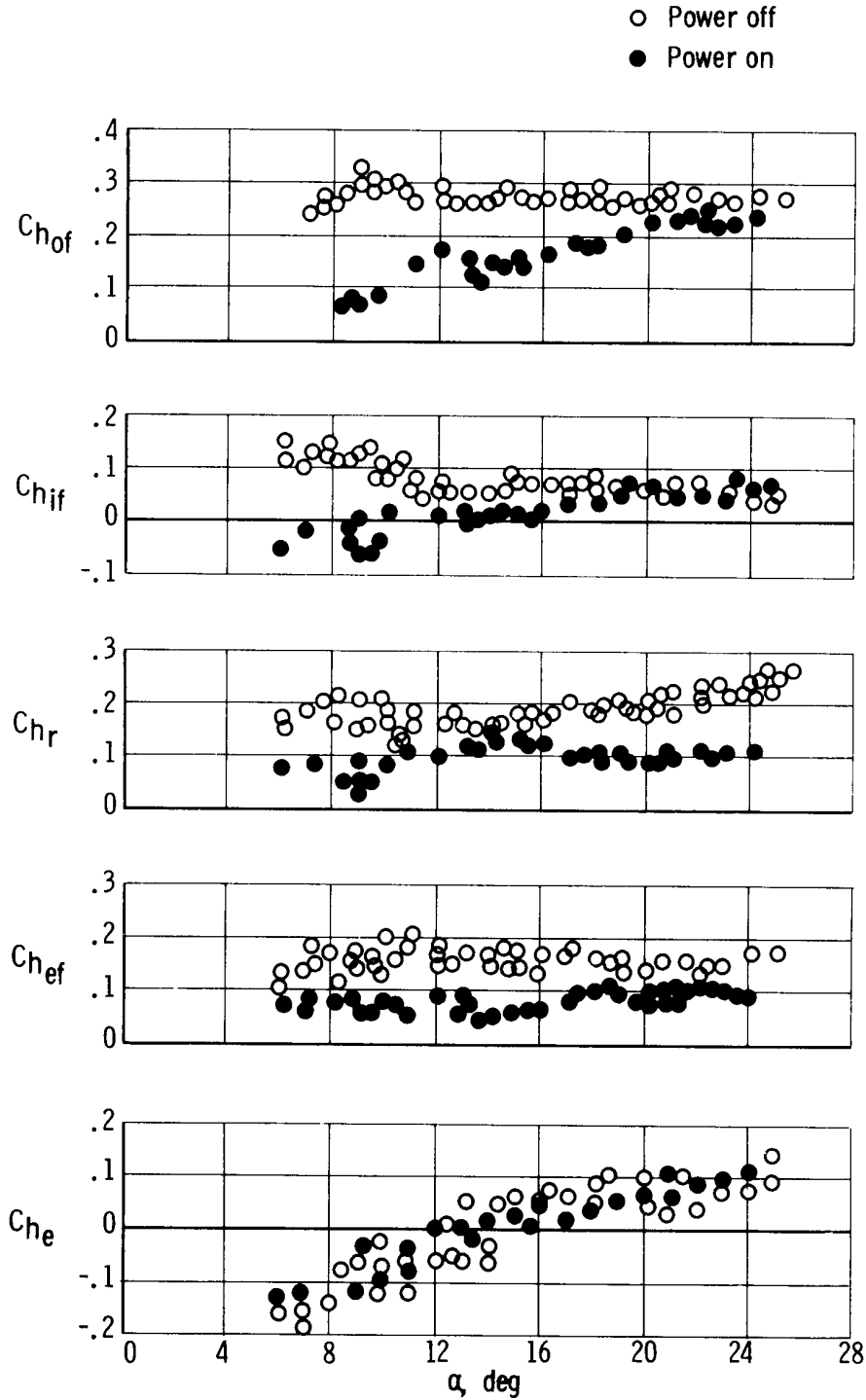


Figure 17. Rocket engine effect on the control surface hinge-moment coefficients.  $\beta = 0^\circ$ ;  $\delta_R = 0^\circ$ ;  $\delta_a = 0^\circ$ ;  $M = 1.2$ ; configuration B. (Control surface deflections shown in figure 2.)